Cell Reports

Article

Myeloid MMP14 couples extracellular proteolysis to inflammatory and metabolic remodeling during obesity

Graphical abstract

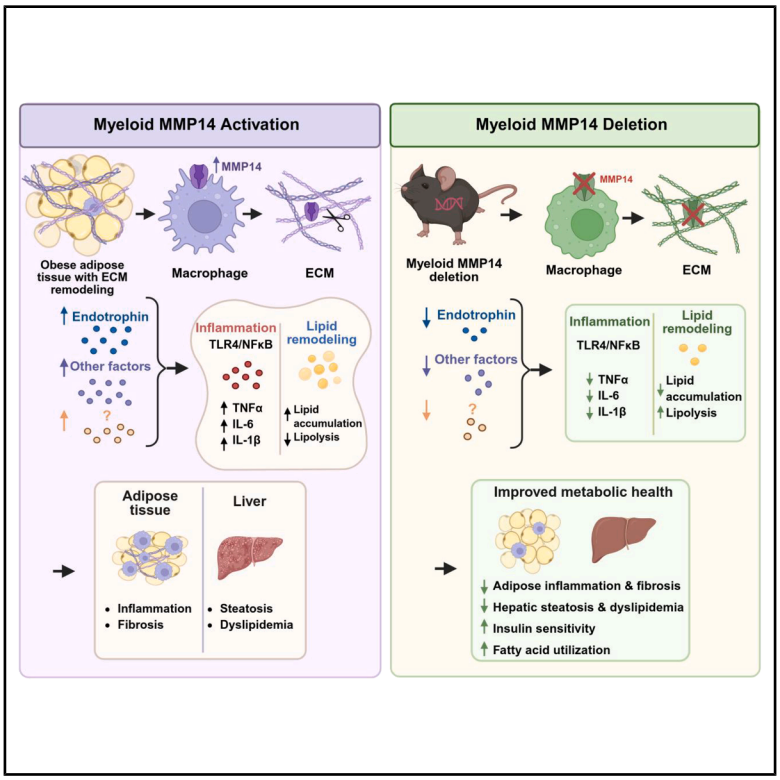

Highlights

- Macrophage MMP14 links matrix remodeling to obesity inflammation via TLR4-NFκB
- Macrophages generate endotrophin via MMP14; it partly mediates inflammation
- MMP14 shapes macrophage lipid metabolism, affecting lipid flux, and cell crosstalk
- Myeloid Mmp14 deletion improves HFD metabolism, lowering inflammation, and steatosis

Authors

Long J. Shao, Fathima Elizondo, Feng Gao, ..., Huaizhu Wu, Sean Hartig, Kai Sun

Correspondence

kai.sun@uth.tmc.edu

In brief

Shao et al. identify macrophage MMP14 as a key regulator linking extracellular matrix proteolysis to inflammatory and metabolic remodeling in obesity. MMP14 promotes endotrophin generation, TLR4-NFκB signaling, and lipid accumulation in macrophages, while myeloid Mmp14 deletion reduces adipose inflammation, fibrosis, hepatic steatosis, and metabolic dysfunction.

Shao et al., 2026, Cell Reports *45*, 117681
July 28, 2026
https://doi.org/10.1016/j.celrep.2026.117681

CellPress

Cell Reports

CellPress
OPEN ACCESS

Article

Myeloid MMP14 couples extracellular proteolysis to inflammatory and metabolic remodeling during obesity

Long J. Shao,[1] Fathima Elizondo,[1] Feng Gao,[2] Elizabeth L. Lieu,[2] Bharati Reddi,[1] Maryam Elizondo,[3] Iqbal Mahmud,[4] Kristin Eckel-Mahan,[1,3] Philipp E. Scherer,[5] Xin Ge,[1,3] Huaizhu Wu,[2] Sean Hartig,[2] and Kai Sun[1,3,6,*]

[1]The Brown Foundation Institute of Molecular Medicine for the Prevention of Human Diseases, University of Texas Health Science Center at Houston, Houston, TX, USA

[2]Department of Medicine, Baylor College of Medicine, Houston, TX, USA

[3]Graduate School of Biomedical Sciences, University of Texas Health Science Center at Houston, Houston, TX, USA

[4]Metabolomics Core Facility, Department of Bioinformatics and Computational Biology, The University of Texas MD Anderson Cancer Center, Houston, TX, USA

[5]Touchstone Diabetes Center, University of Texas Southwestern Medical Center, Dallas, TX, USA

[6]Lead contact

*Correspondence: kai.sun@uth.tmc.edu

https://doi.org/10.1016/j.celrep.2026.117681

SUMMARY

Macrophages orchestrate tissue remodeling, inflammation, and metabolic dysfunction in obesity, but the role of macrophage-intrinsic extracellular proteolysis in immunometabolic regulation remains unclear. Matrix metalloproteinase-14 (MMP14), a membrane-bound protease, is strongly induced during monocyte-to-macrophage differentiation and further elevated in adipose tissue macrophages from high-fat diet (HFD)-fed mice. Pharmacological inhibition or myeloid-specific deletion of Mmp14 impaired macrophage differentiation, proliferation, migration, phagocytosis, and inflammatory activation in response to obesity-associated adipose tissue signals. Mechanistically, MMP14 promoted inflammatory programming by increasing endotrophin generation and enhancing TLR4-NFκB signaling. MMP14 also reprogrammed macrophage lipid metabolism by suppressing lipolysis and promoting lipid accumulation, altering metabolic communication with neighboring cells. *In vivo*, myeloid-specific Mmp14 deletion protected mice from HFD-induced insulin resistance, dyslipidemia, hepatic steatosis, adipose inflammation, and fibrosis. These findings identify macrophage MMP14 as a key mediator linking extracellular matrix remodeling with inflammatory and metabolic dysfunction in obesity.

INTRODUCTION

Obesity induces chronic low-grade inflammation and profound extracellular matrix remodeling in metabolic tissues, including adipose tissue and liver, contributing to insulin resistance, dyslipidemia, and nonalcoholic fatty liver disease.[1–4] Early studies identified tumor necrosis factor-α (TNF-α) as a key inflammatory mediator linking obesity to insulin resistance, establishing inflammation as a central feature of metabolic disease.[5] Subsequent work demonstrated that macrophages accumulate in obese adipose tissue and represent a major source of inflammatory cytokines, directly implicating innate immune cells in metabolic dysfunction.[6–9] In both adipose tissue and liver, macrophages drive inflammatory signaling, fibrosis, and immune cell recruitment, shaping tissue remodeling and disease progression, including enhanced insulin resistance.[10–15] Despite their central role, the macrophage-intrinsic mechanisms that connect ECM remodeling to inflammatory and metabolic dysfunction remain poorly understood.

Matrix metalloproteinases (MMPs) are critical regulators of ECM turnover and immune cell behavior. Beyond degrading structural matrix components, MMPs modulate extracellular signaling by processing cytokines, growth factors, and ECM-derived fragments.[16] Matrix metalloproteinase-14 (MMP14 and MT1-MMP) is a membrane-anchored protease with potent collagenolytic activity and a broad substrate repertoire. MMP14 is essential for pericellular collagen remodeling and activation of pro-MMP2, functions that are critical for localized matrix turnover and tissue invasion.[17–21] Genetic studies established MMP14 as a dominant collagenase *in vivo*, distinguishing it from secreted MMPs in controlling pericellular proteolysis.[22,23]

Several studies have implicated MMP14 in macrophage behavior within matrix-rich tissues. MMP14 enables macrophage migration through dense fibrillar collagen when protease-independent movement is insufficient, allowing macrophages to infiltrate fibrotic or remodeled tissues.[24–27] In disease models, myeloid MMP14 has been linked to macrophage-driven collagen remodeling and inflammation in atherosclerosis and inflammatory

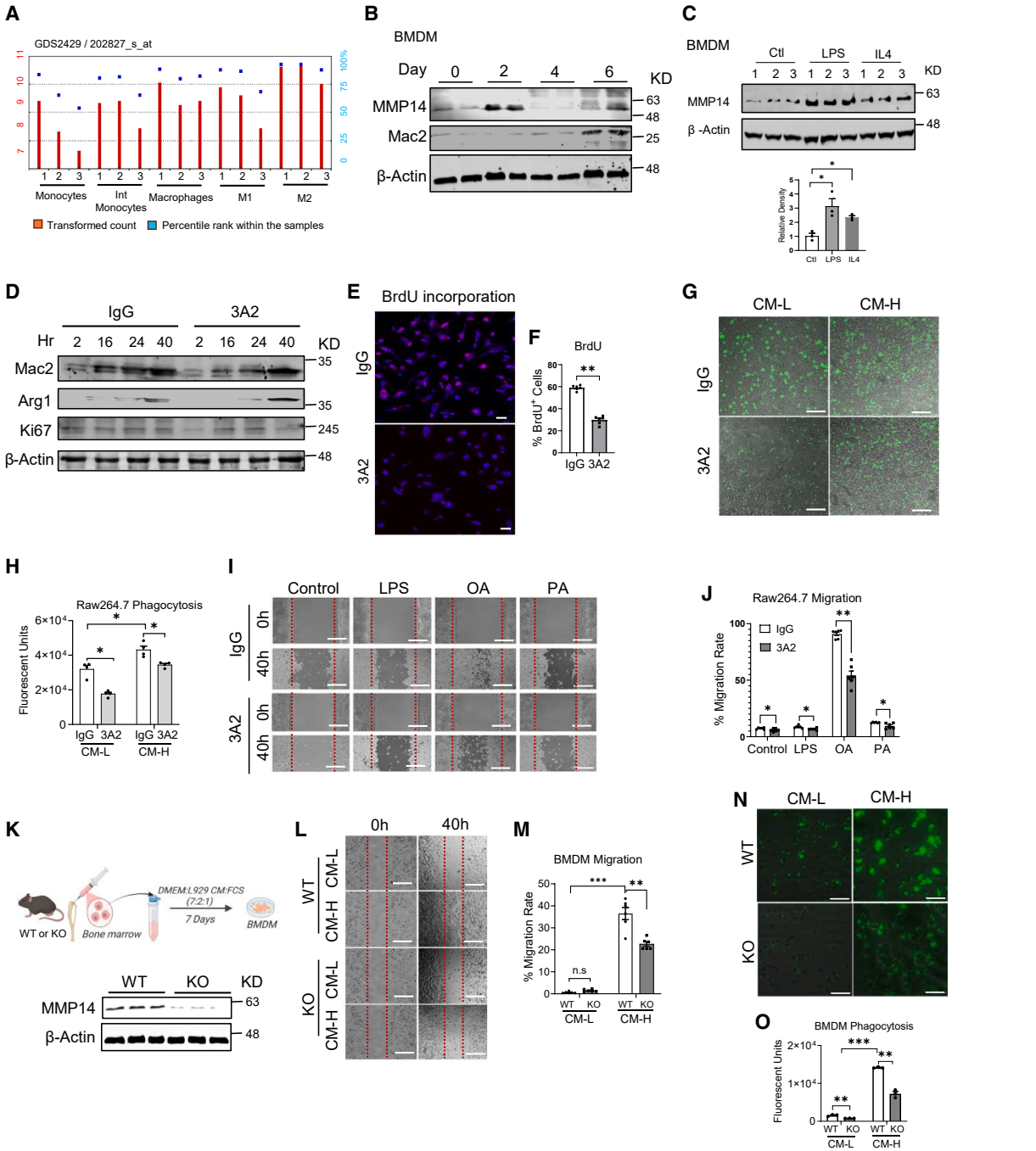

Figure 1. MMP14 expression fluctuates during monocyte-to-macrophage maturation and is required for macrophage differentiation and proliferation

(A) Interrogation of transcriptomic profiles in GEO dataset GDS2429 shows that MMP14 expression undergoes dynamic modulation as circulating monocytes transition to macrophages under M-CSF exposure, and that its levels further shift when these macrophages are driven toward M1-like or M2-like phenotypes by IFN-γ plus LPS or by IL-4 (blue dots indicate percentile rank within the samples).

(B) A temporal assessment of MMP14 and Mac2 expression in bone-marrow-derived monocytes cultured toward macrophages (BMDMs) demonstrates that MMP14 undergoes gradual modulation throughout the differentiation process.

(C) Western blot analysis of MMP14 protein levels in differentiated BMDMs treated with LPS or IL-4. The lower image shows quantification of MMP14 levels normalized to β-actin. Data are presented as mean ± SEM ($n = 3$ per group). One-way ANOVA, followed by Tukey's multiple-comparisons test; $^{*}p < 0.05$.

(D) Blocking MMP14 activity using the MMP14-specific neutralizing antibody 3A2 disrupted THP-1 monocyte differentiation, evidenced by lower levels of Mac2, arginase 1 (Arg1), and Ki67 throughout the progression toward mature macrophages. The protein sample loadings are normalized by β-Actin.

(legend continued on next page)

arthritis,[28–30] and to active construction and remodeling of collagenous matrices in tumors.[31,32] These studies establish MMP14 as a regulator of macrophage localization and tissue architecture. However, they largely view MMP14 as a permissive mediator of matrix remodeling, and do not address whether MMP14 directly programs macrophage inflammatory activation or metabolic state.

ECM remodeling can also generate bioactive fragments, or matrikines, that influence inflammation and metabolism.[33] In obesity, the collagen VI-derived fragment endotrophin has emerged as a key mediator linking fibrosis to metabolic dysfunction.[34–41] Endotrophin was identified as a cleavage product of the collagen VI α3 chain produced by mature adipocytes, where it promotes adipose tissue fibrosis, inflammation, angiogenesis, and systemic insulin resistance.[35,42] This work established ECM-derived signaling as an active driver of metabolic disease. However, endotrophin production has largely been attributed to adipocytes,[2,39] and whether immune cells contribute to its generation, particularly under obesogenic conditions, remains unknown.

Obesity creates a tissue micro-environment characterized by excess lipids, inflammatory stimuli, hypoxia, and progressive ECM accumulation.[2,3,43] In this setting, macrophages adopt specialized inflammatory and metabolic states, marked by lipid accumulation, altered lipid handling, and sustained cytokine production.[44] These obesity-associated macrophages influence adipocyte and hepatocyte metabolism and shape adaptive immune responses, including $CD8^+$ T cell accumulation in obese adipose tissue.[45–49] Although ECM remodeling and lipid overload are defining features of obese tissues, how macrophage-intrinsic ECM proteolysis integrates with lipid metabolism to influence whole-body metabolic outcomes remains unclear.

Here, we uncover a macrophage-intrinsic function of MMP14 that connects extracellular matrix remodeling to inflammatory and metabolic responses in obesity. MMP14 expression rises during monocyte-to-macrophage differentiation and is further increased in macrophages from high-fat diet-fed mice, where it supports macrophage activation, migration, and lipid handling in response to adipose-derived signals. At the mechanistic level, MMP14-dependent matrix processing drives the production of endotrophin, thereby linking between ECM cleavage to macrophage inflammatory signaling. In parallel, MMP14 limits macrophage lipolysis and favors lipid accumulation, thereby influencing both macrophage metabolism and the signals macrophages deliver to neighboring cells. *In vivo*, myeloid deletion of *Mmp14* is associated with improved metabolic outcomes during diet-induced obesity, including reduced lipid burden, a lower inflammatory tone, polarization toward anti-inflammatory and more $TREM2^+$ states, and improved glucose tolerance. Together, these findings suggest that macrophage MMP14, acting in part through endotrophin, couples matrix remodeling to immunometabolic programs that shape tissue remodeling and whole-body metabolic homeostasis.

RESULTS

MMP14 expression is induced during macrophage differentiation and under obesogenic conditions

To determine whether MMP14 expression is regulated during macrophage differentiation and activation, we first examined whether MMP14 expression is regulated during macrophage differentiation. Analysis of publicly available transcriptomic data from GEO dataset GDS2429 showed that MMP14 expression increased as circulating monocytes differentiated into macrophages in response to M-CSF. MMP14 expression was further modulated when macrophages were polarized toward M1-like or M2-like states (Figure 1A), suggesting an association with macrophage differentiation and activation status. To experimentally validate these observations, we assessed

(E) Measurement of THP-1 cell proliferation by confocal imaging. Differentiated THP-1 macrophages were treated with 3A2 or control IgG for 24 h in the presence of BrdU. The images show reduced BrdU incorporation following 3A2 treatment. Scale bar: 10 μm.
(F) Quantification of BrdU incorporation from E. Data are presented as mean ± SEM ($n = 6$ per group), Student's *t* test; $^{**}p < 0.01$.
(G) Phagocytosis in Raw264.7 cells is suppressed by 3A2 treatment. Raw264.7 cells were incubated for 24 h with conditioned medium collected from cultured eWAT (from lean or HFD-fed mice, shown as CM-L and CM-H), together with either 3A2 or control IgG. Phagocytic activity was assessed by the uptake of fluorescent green vesicles. Scale bar: 100 μm.
(H) Quantification of fluorescence intensity of engulfed fluorescent green vesicles. Data are presented as mean ± SEM ($n = 6$ per group), One-way ANOVA, followed by Tukey's multiple-comparisons test; $^{*}p < 0.05$.
(I) Inhibition of MMP14 by 3A2 reduces macrophage migration under various stimuli. Mature Raw264.7 cells were scratched at equal distances across different wells and then treated with various lipids, including OA and PA, as well as the positive control LPS, in the presence of either 3A2 or control IgG for 40 h. Cell migration into the scratched areas was measured to assess macrophage migratory capacity in each condition. The red lines indicate the original scratch boundaries. Scale bar: 200 μm.
(J) Quantification of Raw264.7 cell migration from triplicate experiments using ImageJ software. Data are presented as mean ± SEM ($n = 6$ per group), Student's *t* test; $^{*}p < 0.05$; $^{**}p < 0.01$.
(K) Schematic representation of the process of BMDM isolation from mice (Top); western blotting validates efficient deletion of MMP14 expression on protein levels in the Lysm-Cre-*Mmp14* knockout (KO) mice (Bottom). β-Actin serves as the loading control.
(L) Deletion of *Mmp14* in BMDMs reduces macrophage migratory capacity in response to various stimuli. *Mmp14* KO and wild-type (WT) BMDMs were cultured with conditioned medium collected from HFD-fed eWAT cultures (CM-H) or lean eWAT cultures (CM-L). After 40 h, cell migration in each well was recorded by bright-field imaging. Scale bar: 200 μm.
(M) Quantification of BMDM macrophage migration as shown in L using ImageJ. Data are presented as mean ± SEM ($n = 6$ per group), One-way ANOVA, followed by Tukey's multiple-comparisons test; n.s., not significant; $^{**}p < 0.01$; $^{***}p < 0.001$.
(N) Phagocytosis assays in WT and *Mmp14* KO BMDMs after 24 h of treatment with CM-L or CM-H. Engulfed fluorescent vesicles were visualized by confocal imaging. Scale bar: 100 μm.
(O) Quantification of fluorescence intensity shows that phagocytosis was markedly reduced in KO BMDMs under CM-H treatment conditions. Data are presented as mean ± SEM ($n = 3$ per group), One-way ANOVA, followed by Tukey's multiple-comparisons test; $^{**}p < 0.01$; $^{***}p < 0.001$.

MMP14 expression during the *in vitro* differentiation of mouse bone marrow-derived macrophages (BMDMs). MMP14 expression changed dynamically throughout differentiation and closely paralleled the induction of the macrophage marker Mac2, suggesting that MMP14 is functionally regulated during macrophage differentiation (Figure 1B).

We next asked whether macrophage MMP14 expression is altered in response to different polarization stimuli and under metabolic stress *in vivo*. Differentiated BMDMs were treated with LPS or IL-4 to polarize them toward M1-like or M2-like states, respectively. The results showed that MMP14 protein levels increased in both LPS- and IL-4-treated BMDMs (Figure 1C). Moreover, peritoneal macrophages isolated from mice fed a high-fat diet (HFD) for 16 weeks exhibited markedly elevated MMP14 protein levels compared with macrophages from chow-fed controls (Figure S1A). These data establish that MMP14 expression fluctuates during macrophage differentiation and is further enhanced in macrophages in response to polarization stimuli or exposure to an obesogenic environment.

MMP14 supports macrophage differentiation, proliferation, migration, and phagocytosis

Given the induction of MMP14 during macrophage maturation, we next examined whether MMP14 activity contributes to macrophage differentiation and proliferation. THP-1 monocytes were differentiated in the presence of the MMP14-neutralizing antibody 3A2 (1μg/ml).[42,50] Inhibition of MMP14 reduced the expression of the macrophage differentiation markers Mac2 and Arg1, as well as the proliferation marker Ki67, at multiple observed time points: 2, 16, 24, and 40 h (Figure 1D). To directly assess proliferative capacity, BrdU incorporation assays were performed. Differentiated THP-1 macrophages treated with 3A2 (1μg/ml) exhibited reduced BrdU incorporation compared with IgG-treated controls (Figure 1E), and quantification confirmed a significant reduction in proliferation (Figure 1F).

We next examined whether MMP14 influences macrophage effector functions relevant to tissue remodeling. To achieve this goal, macrophages were treated with conditioned medium (CM) collected from cultured epididymal white adipose tissue (eWAT) obtained from male mice fed either a high-fat diet (CM-H) or a regular chow diet (CM-L).[51] Phagocytic capacity was assessed in Raw264.7 macrophages exposed to CM-L or CM-H. Under both conditions, 3A2-treated macrophages showed reduced uptake of fluorescent vesicles compared with controls, with a more pronounced effect under CM-H conditions (Figure 1G). Quantification further confirmed diminished phagocytic activity (Figure 1H). Macrophage migration was then assessed using scratch assays.[52] Raw264.7 macrophages treated with OA, PA, or LPS exhibited robust migration into the wounded area, whereas migration was consistently reduced in the presence of MMP14 inhibition by 3A2 (Figure 1I), with quantification demonstrating decreased wound closure across all stimuli (Figure 1J).

To validate these findings genetically, BMDMs isolated from LysM-Cre-*Mmp14* KO mice (Figure 1K; Figure S1G) were examined. Compared with WT macrophages, *Mmp14* KO BMDMs exhibited reduced migration in response to CM-L and CM-H, with a more pronounced defect under CM-H conditions (Figures 1L–1M). Phagocytic capacity was also significantly reduced in *Mmp14* KO BMDMs under both conditions, with a more pronounced defect under CM-H conditions (Figures 1N–1O). Together, these results indicate that MMP14 activity supports macrophage differentiation, proliferation, migration, and phagocytosis.

MMP14 is required for pro-inflammatory macrophage polarization and inflammatory signaling

Because macrophages in obese tissues are exposed to adipose-derived inflammatory cues,[53] we next examined whether MMP14 regulates macrophage polarization in response to these signals. Raw264.7 macrophages treated with CM-L exhibited a modest increase in $CD86^+$ M1-like macrophages, which was reduced by MMP14 inhibition with 3A2 (Figures 2A and 2B; Figure S2). When macrophages were treated with CM-H, a more pronounced expansion of $CD86^+$ was observed in the macrophages. This CM-H-induced pro-inflammatory polarization was significantly attenuated in the presence of 3A2 (Figures 2C and 2D). In contrast, the anti-inflammatory polarization population ($CD206^+$) was increased in 3A2-treated macrophages under CM-L conditions (Figures 2A and 2B). However, no significant differences were observed under CM-H conditions, in which the $CD206^+$ population was reduced to very low levels in both groups (Figures 2C and 2D). Quantification of the polarizations were shown in Figure 2E.

We then examined primary macrophages from WT and MMP14 KO mice. Compared with the WT, KO BMDMs treated with CM-L showed reduced proportions of $F4/80^+CD86^+$ (M1-like) and increased portion of $F4/80^+CD206^+$ (M2-like) macrophages (Figures 2F and 2G). Under CM-H conditions, WT macrophages exhibited a strong shift toward the M1-like phenotype, whereas *Mmp14* KO macrophages failed to mount a comparable response. In contrast, M2-like macrophage populations were not significantly altered by MMP14 loss under CM-H conditions (Figures 2H and 2I). Quantification of the polarizations were shown in Figure 2J.

To determine whether the observed changes in macrophage polarization were accompanied by alterations in inflammatory signaling, we next examined expression of key pathway components, including TLR4, NF-κB, TNFα, IL-1β, and IL-6. In Raw264.7 macrophages, treatment with adipose tissue-derived conditioned media induced expression of these inflammatory markers, and this induction was reduced by MMP14 neutralization with 3A2 under both CM-L and CM-H conditions, with a more pronounced reduction under CM-H conditions (Figures 2K and 2L). Importantly, the secretion of IL-1β, IL-6, and TNFα into the culture media showed a similar pattern of changes, particularly under CM-H conditions (Figure 2M).

Similarly, Raw264.7 cells were treated with LPS in the presence or absence of 3A2, followed by western blot analysis. Consistent results were observed for these inflammatory factors (Figures 1B and 1C). ELISA assays further confirmed similar changes in their secreted levels, resembling the pattern observed under CM-H treatment. Interestingly, no significant changes in these pro-inflammatory factors were observed under IL-4 treatment conditions (Figures S1D–S1F).

To further assess inflammatory signaling at the subcellular level, NF-κB localization was examined by immunofluorescent

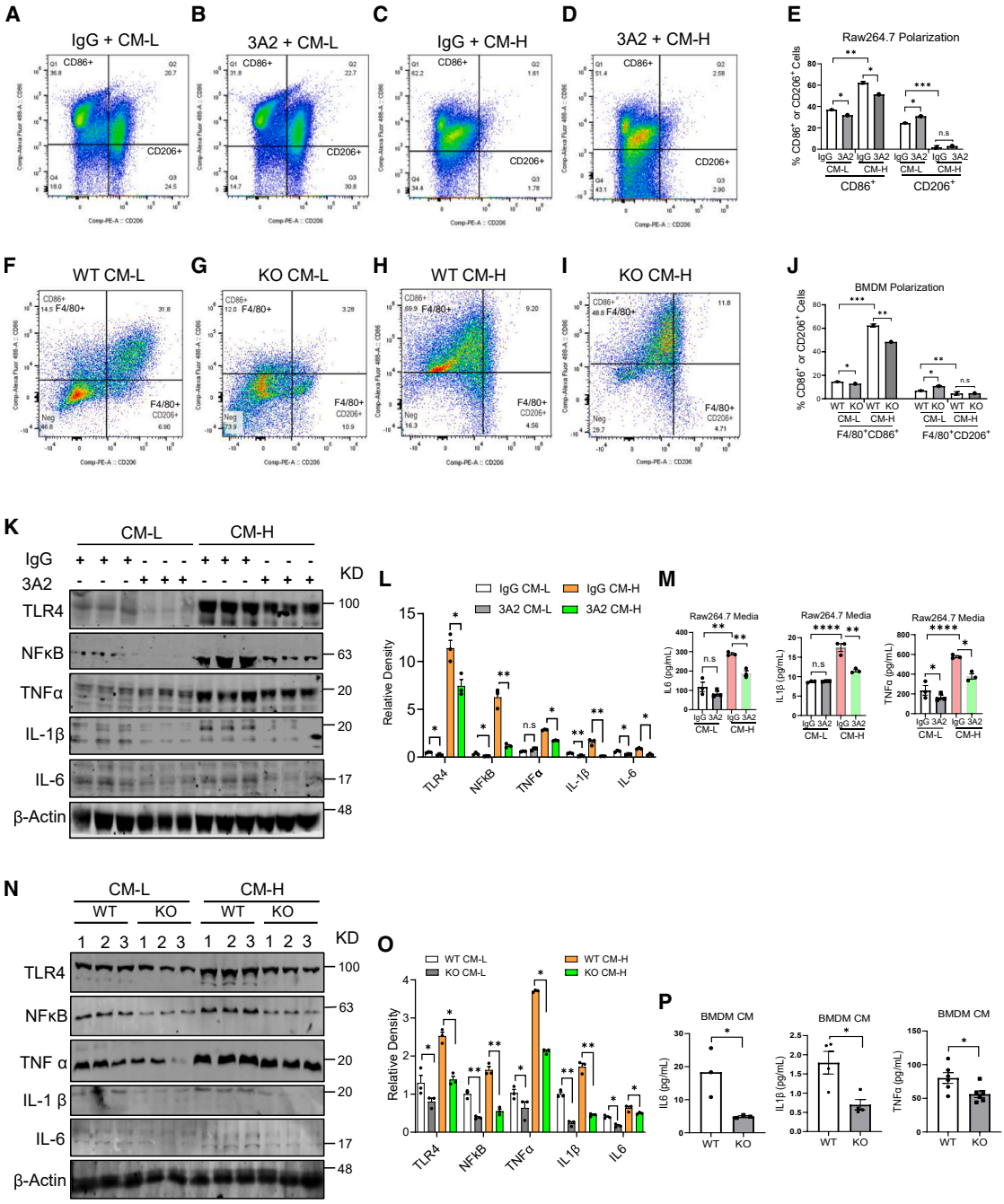

Figure 2. Conditioned media from HFD eWAT reveals a role for MMP14 in driving pro-inflammatory macrophage activation

(A and B) Flow cytometry analysis of M1-like (CD86$^+$) and M2-like (CD206$^+$) macrophage populations in Raw264.7 cells treated with CM-L in the presence of either 3A2 or control IgG.

(C and D) Flow cytometry analysis of M1-like (CD86$^+$) and M2-like (CD206$^+$) macrophage populations in Raw264.7 cells treated with CM-H in the presence of either 3A2 or control IgG.

(E) Quantification of CD86$^+$ and CD206$^+$ macrophage populations. Data are presented as mean ± SEM (n = 3). One-way ANOVA, followed by Tukey's multiple-comparisons test; n.s., not significant; *$p < 0.05$; **$p < 0.01$.

(F and G) Flow cytometry analysis of M1-like (F4/80$^+$CD86$^+$) and M2-like (F4/80$^+$CD206$^+$) macrophage populations in WT and *Mmp14* KO BMDMs treated with CM-L.

(H and I) Flow cytometry analysis of M1-like (F4/80$^+$CD86$^+$) and M2-like (F4/80$^+$CD206$^+$) macrophage populations in WT and *Mmp14* KO BMDMs treated with CM-H.

(legend continued on next page)

staining. Compared with CM-L treatment, CM-H markedly increased total NF-κB signal intensity in Raw264.7 macrophages (Figure S3A). Notably, CM-H treatment also promoted nuclear accumulation of NF-κB, consistent with activation of NFκB-dependent transcriptional programs. Treatment with the MMP14-neutralizing antibody 3A2 reduced overall NF-κB signal intensity and substantially decreased nuclear localization of NF-κB under CM-H conditions (Figure S3A).

We then asked whether *Mmp14* KO primary macrophages produced a similar effect. In WT BMDMs, both CM-L and CM-H induced the expression of TLR4, NF-κB, TNFα, IL-1β, and IL-6, with stronger induction observed under CM-H conditions. In contrast, induction of these inflammatory proteins was markedly reduced in *Mmp14* KO BMDMs (Figures 2N and 2O). CM-H treatment also promoted nuclear accumulation of NF-κB in WT BMDMs, consistent with activation of NFκB-dependent transcriptional programs. The treatment further reduced overall NF-κB signal intensity and substantially decreased nuclear localization of NF-κB in *Mmp14* KO BMDMs (Figure S3B). Moreover, under CM-H conditions, secreted IL-6, IL-1β, and TNFα levels were significantly reduced in conditioned media from *Mmp14* KO BMDMs (Figure 2P).

MMP14 regulates lipid accumulation and lipid metabolic programs in macrophages

Having observed that MMP14 promotes pro-inflammatory macrophage activation in response to adipose-derived signals, we next asked whether MMP14 also regulates macrophage lipid handling, a defining feature of obesity-associated macrophages. To address this, we first examined lipid accumulation in macrophages under defined lipid-loading conditions. Raw264.7 macrophages were treated with oleic acid (OA), palmitic acid (PA), or a combination of OA and PA. Measurement of intracellular triglyceride (TAG) levels revealed that neutralization of MMP14 with the antibody 3A2 reduced TAG accumulation under all lipid-loading conditions compared with IgG-treated controls (Figure 3A). We next examined intracellular free fatty acid (FFA) levels in the same experimental setting. Raw264.7 macrophages treated with 3A2 exhibited increased intracellular FFA levels compared with control-treated cells (Figure 3B), suggesting altered lipid turnover rather than increased lipid storage.

To assess macrophage lipid accumulation in response to oxidized lipids, Raw264.7 macrophages were treated with oxidized LDL (oxLDL). BODIPY staining showed that oxLDL treatment induced robust lipid droplet accumulation compared with untreated controls (Figure 3C, upper panels). Treatment with the MMP14-neutralizing antibody 3A2 markedly reduced oxLDL-induced lipid droplet accumulation (Figure 3C, upper panels). Quantification of BODIPY fluorescence intensity confirmed a significant decrease in lipid accumulation following 3A2 treatment (Figure 3C, lower panels).

To examine whether adipose tissue-derived factors modulate macrophage lipid accumulation in an MMP14-dependent manner, Raw264.7 macrophages were treated with CM-L or CM-H. BODIPY staining showed that CM-H treatment markedly increased lipid droplet accumulation compared with CM-L, whereas CM-L treatment alone had minimal effects (Figure 3D, upper panels). Treatment with the MMP14-neutralizing antibody 3A2 substantially reduced CM-H-induced lipid droplet accumulation, while having little effect under CM-L conditions (Figure 3D, upper panels). Quantification of BODIPY fluorescence intensity confirmed a significant reduction in lipid accumulation following 3A2 treatment under CM-H conditions (Figure 3D, lower panels).

Subsequently, we tested whether genetic deletion of MMP14 in primary macrophages produces similar effects. BMDMs from WT and *Mmp14* KO mice were treated with CM-L or CM-H. Under CM-H conditions, *Mmp14* KO macrophages exhibited reduced intracellular TAG levels compared with WT macrophages (Figure 3E). Intracellular FFA levels were also reduced in *Mmp14* KO macrophages (Figure 3F). Consistent with these biochemical changes, BODIPY staining revealed reduced lipid droplet accumulation in *Mmp14* KO macrophages (Figure 3G).

To define the molecular basis for altered lipid accumulation, we examined expression of key lipid metabolic regulators. Immunoblot analysis further showed increased expression of ATGL and HSL, along with elevated *p*-ACC and decreased total ACC, in Mmp14 KO macrophages under both CM-L and CM-H conditions, with more pronounced effects observed under CM-H conditions (Figures 3H–3J). Together, these findings indicate reduced *de novo* lipogenesis and increased lipolytic activity in *Mmp14* KO BMDMs.

MMP14-dependent macrophage signals influence lipid accumulation in recipient cells

Because macrophages communicate metabolic signals to surrounding cells,[54–56] we asked whether MMP14-dependent

(J) Quantification of F4/80$^+$CD86$^+$ and F4/80$^+$CD206$^+$ macrophage populations. Data are presented as mean ± SEM (n = 3). One-way ANOVA, followed by Tukey's multiple-comparisons test; n.s., not significant; $^*p < 0.05$; $^{**}p < 0.01$, $^{***}p < 0.001$.

(K) Western blot analysis of Raw264.7 cells treated with CM-L or CM-H in the presence or absence of 3A2 or control IgG. Detected pro-inflammatory factors: TLR4, NF-κB, TNFα, IL-1β, and IL-6. β-Actin was used as a loading control.

(L) Quantification of band intensities using ImageJ, shown in K. Data are presented as mean ± SEM (n = 3). One-way ANOVA, followed by Tukey's multiple-comparisons test; n.s., not significant; $^*p < 0.05$; $^{**}p < 0.01$.

(M) ELISA analysis of culture media from Raw264.7 cells treated with CM-L or CM-H in the presence of 3A2 or control IgG. Detected pro-inflammatory factors: TNFα, IL-1β, and IL-6. Statistical significance was determined by one-way ANOVA followed by Tukey's multiple-comparisons test. n.s., not significant; $^*p < 0.05$; $^{**}p < 0.01$; $^{****}p < 0.0001$.

(N) Western blot analysis of WT and MMP14 KO BMDMs treated with CM-L or CM-H, detecting TLR4, NF-κB, TNFα, IL-1β, and IL-6. β-Actin served as a loading control.

(O) Quantification of band intensities shown in N. Data are presented as mean ± SEM (n = 3). Statistical significance was determined by one-way ANOVA followed by Tukey's multiple-comparisons test. $^*p < 0.05$; $^{**}p < 0.01$.

(P) ELISA analysis of culture media from WT and *Mmp14* KO cells treated with CM-H. Detected pro-inflammatory factors: TNFα, IL-1β, and IL-6. Statistical significance was determined by Student's t test. $^*p < 0.05$.

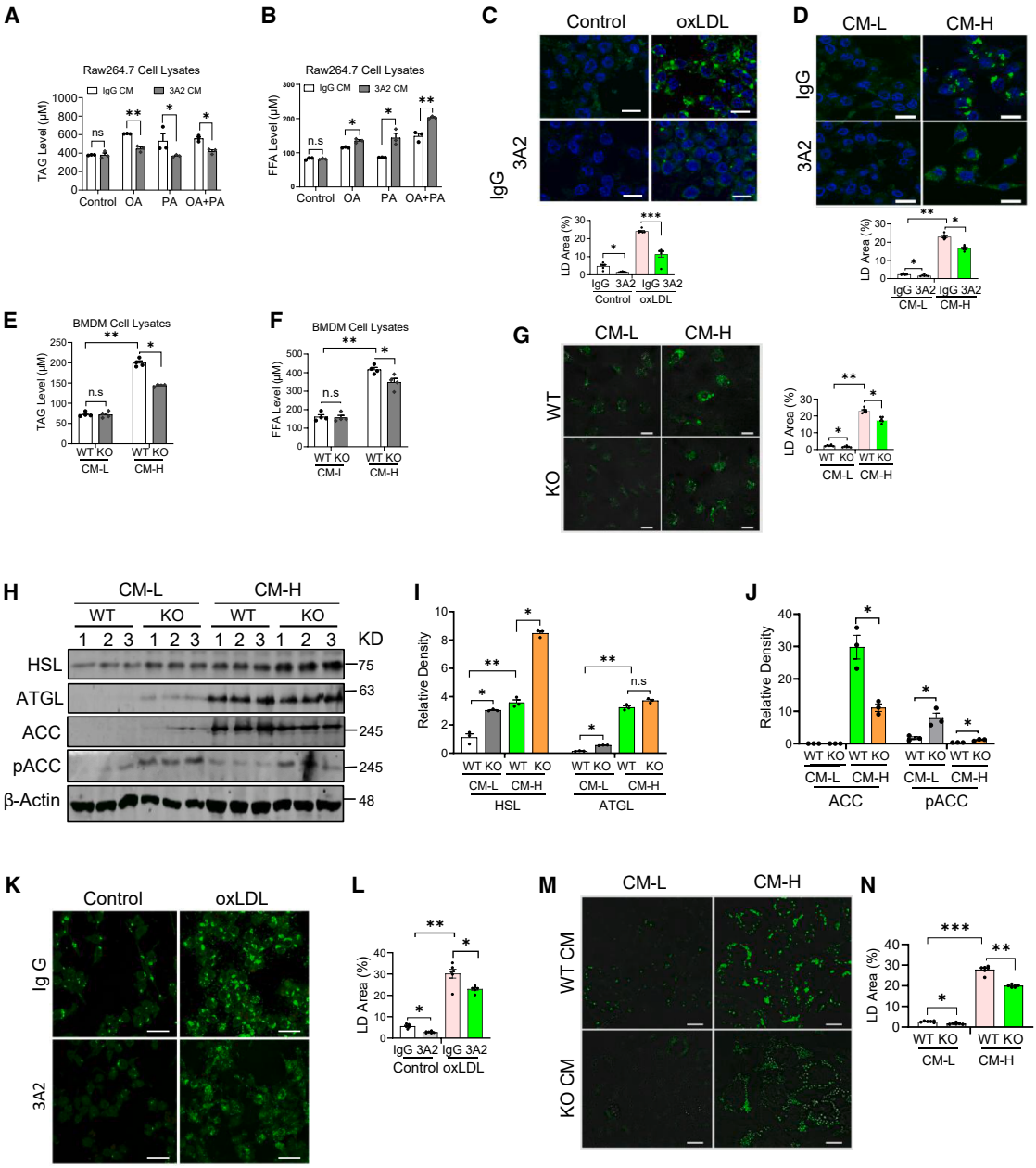

Figure 3. MMP14 deficiency reduces macrophage lipid accumulation and alters lipid metabolism

(A and B) Triacylglycerol (TAG) (A) or free fatty acid (FFA) levels (B) level in Raw264.7 cells treated with OA, PA, or OA + PA in the presence or absence of 3A2 or control IgG. Data are presented as mean ± SEM ($n = 3$), Student's t test; n.s., not significant; $^{*}p < 0.05$, $^{**}p < 0.01$.

(C) Confocal images of BODIPY fluorescence staining in Raw264.7 cells treated with or without oxLDL in the presence of 3A2 or control IgG. The bottom image shows quantification of fluorescence intensity from the images shown in the upper image. Data are presented as mean ± SEM ($n = 3$ fields). Scale bar: 10 μm. Statistical significance was determined by one-way ANOVA followed by Tukey's multiple-comparisons test. $^{*}p < 0.05$; $^{***}p < 0.001$.

(D) Confocal images of BODIPY fluorescence staining in Raw264.7 cells treated with CM-L or CM-H, together with 3A2 or control IgG. The bottom image shows quantification of fluorescence intensity from the images shown in the upper image. Data are presented as mean ± SEM ($n = 3$ fields). Scale bar: 10 μm. Statistical significance was determined by one-way ANOVA followed by Tukey's multiple-comparisons test. $^{*}p < 0.05$, $^{**}p < 0.01$).

(E and F) TAG (E) and FFA (F) levels in WT and KO BMDMs treated with CM-L or CM-H. Data are presented as mean ± SEM ($n = 4$). Statistical significance was determined by one-way ANOVA followed by Tukey's multiple-comparisons test. n.s., not significant; $^{*}p < 0.05$, $^{**}p < 0.01$.

(G) Representative confocal images of BODIPY fluorescence in WT and KO BMDMs treated with CM-L) or CM-H. The right image shows quantification of fluorescence intensity. Data are presented as mean ± SEM ($n = 6$). Scale bar: 10 μm. Statistical significance was determined by one-way ANOVA followed by Tukey's multiple-comparisons test. n.s., not significant; $^{*}p < 0.05$, $^{**}p < 0.01$.

(legend continued on next page)

changes in macrophage lipid metabolism influence lipid accumulation in recipient cells. To test this, conditioned media transfer experiments were performed using AML hepatocyte-like cells. AML cells exposed to conditioned media from oxLDL-treated Raw264.7 macrophages accumulated abundant lipid droplets, as visualized by BODIPY staining (Figure 3K). In contrast, AML cells treated with conditioned media from Raw264.7 macrophages treated with oxLDL in the presence of 3A2 exhibited markedly reduced lipid accumulation (Figures 3K and 3L). To determine whether genetic ablation of *Mmp14* in macrophages alters macrophage-dependent regulation of lipid accumulation in recipient cells, AML cells were treated with conditioned media collected from WT or *Mmp14* KO BMDMs cultured by lean CM-L or CM-H. BODIPY staining showed that AML cells treated with conditioned media from *Mmp14* KO BMDMs under CM-H conditions exhibited markedly reduced lipid droplet accumulation compared with those treated with WT-derived CM-H conditioned media, while no appreciable difference was observed under CM-L conditions (Figures 3M and 3N).

MMP14 regulates endotrophin production and downstream inflammatory and metabolic gene programs

MMP14 is known to cleave collagen VI in adipocytes to generate endotrophin, a matrikine directly linked to metabolic inflammation.[40,42,57] Both endogenous and secreted endotrophin have been shown to exert profound fibrotic and pro-inflammatory effects by activating distinct signaling pathways.[35,40,57,58] To determine whether MMP14 regulates endotrophin production in macrophages, Raw264.7 cells were treated with CM-L or CM-H in the presence of control IgG or 3A2. Immunoblot analysis showed that endotrophin was detectable in macrophages treated with CM-L, and this basal endotrophin production was reduced by 3A2 treatment (Figure 4A). CM-H treatment induced higher levels of endotrophin, and this CM-H-induced endotrophin production was also inhibited by 3A2 (Figures 4A and 4B). ELISA using an endotrophin-specific antibody further confirmed that, under CM-H conditions, inhibition of MMP14 with 3A2 reduced endotrophin production in the culture media (Figure 4C). To assess whether *Mmp14* KO affects endotrophin production in macrophages, WT and *Mmp14* KO BMDMs were treated with CM-L or CM-H. Immunoblot analysis showed that WT BMDMs produced detectable levels of endotrophin under CM-L conditions, whereas endotrophin levels were significantly reduced in *Mmp14* KO BMDMs (Figure 4D). CM-H treatment induced higher endotrophin production, and this induction was markedly blunted in *Mmp14* KO BMDMs (Figures 4D and 4E). ELISA using an endotrophin-specific antibody further confirmed that, under both CM-L and CM-H conditions, endotrophin production was significantly reduced in culture media collected from Mmp14 KO BMDMs, with a more pronounced reduction under CM-H conditions (Figure 4F).

To determine whether endotrophin mediates MMP14-dependent inflammatory signaling in macrophages, Raw264.7 cells were treated with the MMP14-neutralizing antibody 3A2 in the presence or absence of recombinant endotrophin. Immunoblot analysis showed that 3A2 treatment suppressed the expression of the indicated pro-inflammatory factors, including TNFα, IL-6, and IL-1β (Figure 4G). Importantly, addition of endotrophin restored the expression levels of these pro-inflammatory proteins (Figures 4G and 4H). Similar rescue effects were observed in *Mmp14* KO BMDMs treated with endotrophin (Figure 4I).

Transcriptomic profiling reveals MMP14-dependent regulation of inflammatory and lipid metabolism pathways

To define broader transcriptional programs regulated by MMP14, we performed RNA-seq analysis on Raw264.7 macrophages treated with LPS in the presence or absence of the MMP14-neutralizing antibody 3A2 (Figure S4). Unbiased transcriptomic profiling identified widespread changes in gene expression, with hundreds of genes differentially regulated following MMP14 inhibition. Heatmap analysis highlighted coordinated downregulation of inflammatory gene networks (Figure 4J) as well as genes associated with macrophage proliferation and cell cycle regulation (Figure 4K). In parallel, pathway-focused analysis revealed suppression of lipogenesis-related gene programs and enrichment of genes involved in lipid catabolic processes, including lipolysis (Figures 4L and 4M). A GO/pathway enrichment analysis further highlighted the selected upregulated genes, including the proinflammatory markers, such as selected significantly changed genes, such as *Il23a*, *Tnfaip3*, *Tnfaip2*, *Tnfsf10b*, and *Tnfsf13b* (Figure 4N).

To validate these RNA-seq findings, we performed RT-qPCR analysis of selected representative genes. Consistent with the transcriptomic data, expression of key inflammatory and macrophage activation genes (*Tlr4*, *NF-κB*, *IL-6*, *Il1b*, and *Tnfα*) was

(H) Western blots of protein lysates from WT and KO BMDMs treated with CM-L or CM-H. Lipid-metabolism–related proteins analyzed include ACC/p-ACC, ATGL, and HSL. β-Actin was used as the loading control.
(I) Quantification of band intensities for ATGL and HSL in (H). Data are presented as mean ± SEM ($n = 3$). Statistical significance was determined by one-way ANOVA followed by Tukey's multiple-comparisons test. n.s., not significant; $^{*}p < 0.05$, $^{**}p < 0.01$.
(J) Quantification of the band intensities for ACC and *p*-ACC in (H). Data are presented as mean ± SEM ($n = 3$). Statistical significance was determined by one-way ANOVA followed by Tukey's multiple-comparisons test. $^{*}p < 0.05$.
(K) Representative BODIPY fluorescence images of AML cells treated with conditioned media from Raw264.7 cells co-treated with oxLDL and 3A2 or IgG control. Scale bar: 10 μm.
(L) Quantification of BODIPY fluorescence intensity shown in (K). Six fields were analyzed per group. Data are presented as mean ± SEM ($n = 6$). Statistical significance was determined by one-way ANOVA followed by Tukey's multiple-comparisons test. $^{*}p < 0.05$, $^{**}p < 0.01$.
(M) Representative BODIPY fluorescence images of AML cells treated with conditioned media from WT or KO BMDMs exposed to CM-L) or CM-H conditioned media. Scale bar: 10 μm.
(N) Quantification of BODIPY fluorescence intensity is shown in (M). Six fields were analyzed per group. Data are presented as mean ± SEM ($n = 6$). Statistical significance was determined by one-way ANOVA followed by Tukey's multiple-comparisons test. $^{*}p < 0.05$, $^{**}p < 0.01$, $^{***}p < 0.001$.

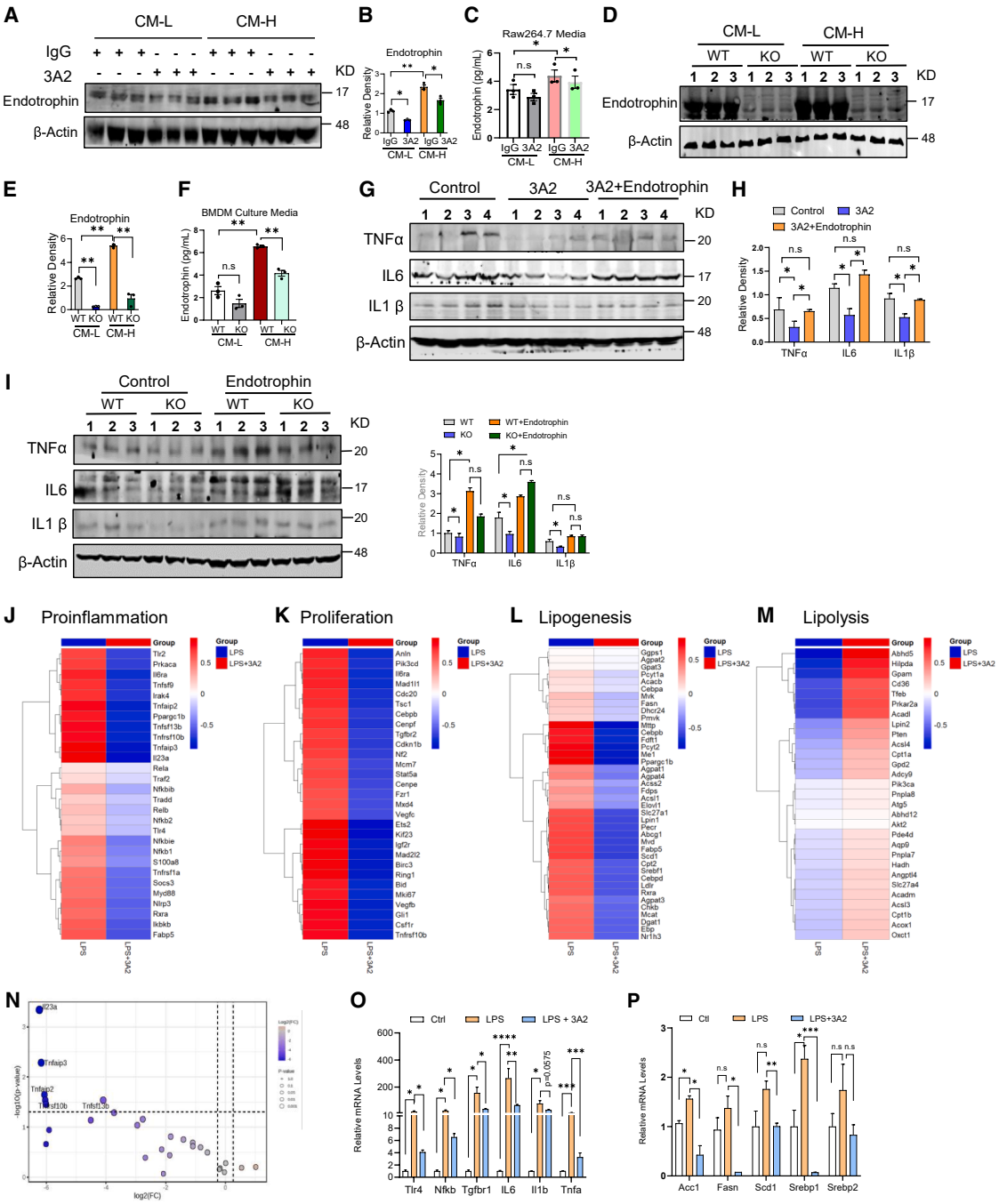

Figure 4. Suppression of MMP14 reduces endotrophin under inflammatory and adipose tissue-derived stimuli

(A) Western blot analysis of endotrophin in Raw264.7 macrophages treated with 3A2 or control IgG. β-Actin was loaded as the loading control (same loading control as in Figure 2K).

(B) Quantification of endotrophin band intensity in (A). Data are presented as mean ± SEM ($n = 3$). Statistical significance was determined by one-way ANOVA followed by Tukey's multiple-comparisons test. *$p < 0.05$.

(C) ELISA analysis of secreted endotrophin in culture media from Raw264.7 cells treated with 3A2 or control IgG. Statistical significance was determined by one-way ANOVA followed by Tukey's multiple-comparisons test. n.s., not significant; *$p < 0.05$.

(D) Western blot analysis of endotrophin in WT and *Mmp14* KO BMDM macrophages treated with CM-H or CM-L. β-Actin was loaded as the loading control.

(E) Quantification of endotrophin band intensity in (D). Data are presented as mean ± SEM ($n = 3$). Statistical significance was determined by one-way ANOVA followed by Tukey's multiple-comparisons test. *$p < 0.05$, **$p < 0.01$.

(F) ELISA analysis of secreted endotrophin in culture media from WT and *Mmp14* KO BMDM treated with CM-L or CM-H. Statistical significance was determined by one-way ANOVA followed by Tukey's multiple-comparisons test. n.s., not significant; **$p < 0.01$.

(legend continued on next page)

significantly downregulated following MMP14 inhibition (Figure 4O). Likewise, expression of representative lipogenesis-related genes (*Acc1*, *Fasn*, *Scd1*, and *Srebp2*) was downregulated (Figure 4P), confirming the reliability of the RNA-seq results.

Myeloid *Mmp14* deletion improves systemic metabolic homeostasis during HFD feeding

To determine whether the macrophage-intrinsic effects of MMP14 observed *in vitro* translate into systemic metabolic outcomes *in vivo*, WT and *Mmp14* KO mice were fed an HFD for 16 weeks. Body weight gain over time was comparable between genotypes, and no significant differences in total body weight were observed at any time point during the feeding period (Figure 5A). Because similar body weight does not necessarily reflect comparable body composition, we next evaluated fat and lean mass. Compared with WT controls, *Mmp14* KO mice showed a reduced fat mass and a corresponding tendency toward increased lean mass (Figures 5B and 5C).

We next assessed glucose homeostasis. Fasting glucose levels were reduced in *Mmp14* KO mice (Figure 5D). To further evaluate glucose homeostasis, mice were subjected to an intraperitoneal glucose tolerance test (IPGTT). *Mmp14* KO mice displayed improved glucose clearance following intraperitoneal glucose administration compared with WT controls (Figure 5E), with quantification shown in Figure 5F. To assess systemic insulin sensitivity, mice were next subjected to an insulin tolerance test (ITT). Blood glucose responses during ITT were comparable between WT and *Mmp14* KO mice (Figure 5G), and quantification confirmed no significant difference between genotypes (Figure 5H).

Systemic lipid parameters were then examined. Circulating TAG levels were reduced in *Mmp14* KO mice (Figure 5I), whereas circulating FFA levels were unchanged (Figure 5J). TAG content was reduced in eWAT (Figure 5K) and liver (Figure 5M), whereas tissue FFA levels were unchanged (Figure 5L). Circulating inflammatory cytokines, including *m*-CSF, were reduced in *Mmp14* KO mice (Figure 5N).

Circulating and tissue inflammatory factors were measured using specific ELISA assays. The results showed no significant differences in circulating IL-6, IL-1β, or TNFα levels between WT and *Mmp14* KO mice; however, all three factors were significantly reduced in the eWAT of *Mmp14* KO mice (Figures S5A–5C; Figures 5O–5Q). Notably, both circulating and local eWAT endotrophin levels were dramatically decreased in Mmp14 KO mice, as measured by ELISA (Figures 5R and 5S).

To determine whether the metabolic improvements observed in *Mmp14* KO mice were accompanied by alterations in whole-body energy metabolism, indirect calorimetry was performed following HFD feeding. Oxygen consumption (VO_2) and carbon dioxide production (VCO_2) were continuously monitored. *Mmp14* KO mice exhibited significantly increased CO_2 production (VCO_2) during the light phase compared with WT controls (Figures S5F and 5G). Although VO_2 during the light phase and both VO_2 and VCO_2 during dark phase showed an upward trend in KO mice, these differences did not reach statistical significance (Figures 5D–5G). Consistent with these findings, heat production in *Mmp14* KO mice showed a tendency to increase during both the dark phase; however, the difference did not reach statistical significance compared with WT controls (Figures 5H and 5I). To assess substrate utilization, respiratory exchange ratio (RER) was analyzed. *Mmp14* KO mice displayed a significant shift toward lower RER values, suggesting increased reliance on fatty acid oxidation (Figures 5T and 5U).

Myeloid Mmp14 deletion drives tissue-level lipid metabolic remodeling

We next examined whether myeloid *Mmp14* deletion is associated with coordinated changes in lipid metabolism and tissue morphology across key metabolic organs. To address this, histological and molecular analyses were performed in WAT, liver, and brown adipose tissue (BAT) following HFD feeding. H&E staining revealed reduced adipocyte hypertrophy in both subcutaneous WAT (sWAT) and eWAT from *Mmp14* KO mice compared with WT controls (Figure 6A). In addition, BAT from Mmp14 KO mice exhibited improved morphology characterized by a more multilocular appearance, and liver sections showed reduced lipid accumulation relative to WT mice (Figure 6A). Quantification of adipocyte size across the indicated adipose

(G) Western blot analysis of pro-inflammatory factors (TNFα, IL-6, and IL-1β) in Raw264.7 cells treated with control IgG, 3A2 alone, or in combination with endotrophin (1μg/ml).

(H) Quantification of band intensities in (G). Data are presented as mean ± SEM ($n = 4$). Statistical significance was determined by one-way ANOVA followed by Tukey's multiple-comparisons test. n.s., not significant; *$p < 0.05$.

(I) Western blot analysis of pro-inflammatory factors (TNFα, IL-6, and IL-1β) in WT and KO BMDMs treated with control IgG or endotrophin (1 1 μg/ml). Quantification of band intensities: Data are presented as mean ± SEM ($n = 3$ per group). Analyzed using one-way ANOVA followed by Tukey's multiple-comparisons test. n.s., not significant; *$p < 0.05$.

(J–M) Heatmap of differentially expressed genes (DEGs) highlighting MMP14-dependent regulation of pro-inflammatory, proliferation, lipogenesis, and lipolysis pathways in the Raw264.7 cells treated by LPS (100 ng/mL) for 24 h. $n = 3$ per group, shown as the average of three replicates. Pathway enrichment analysis was conducted using gene set enrichment analysis (GSEA). All comparisons: unpaired, two tailed Student's *t* test. Proinflammatory signature $p = 4.45E{-}16$; proliferation signature $p = 2.32E{-}41$; lipogenesis signature *p* value $8.22E{-}15$; lipolysis signature $p = 1.29E{-}05$.

(N) Gene ontology (GO) and pathway enrichment analyses identifying major pathways suppressed or enhanced by MMP14 neutralization, highlighting the proinflammatory program.

(O) RT-qPCR validation of representative DEGs identified by RNA-seq. Expressions of inflammation- and macrophage activation-related genes (Tlr4, Nfkb, IL-6, Il1b, and Tnfa) were consistent with RNA-seq results, confirming dataset reliability. $n = 3$ per group. Data were analyzed using one-way ANOVA; n.s., not significant; *$p < 0.05$; **$p < 0.01$; ***$p < 0.001$, ****$p < 0.0001$.

(P) RT-qPCR validation of representative DEGs identified by RNA-seq. Expressions of lipogenesis-related genes (Acc1, Fasn, Scd1, Srebp1, and Srebp2) were consistent with RNA-seq results, confirming dataset reliability. $n = 3$ per group. Data were analyzed using one-way ANOVA; n.s., not significant; *$p < 0.05$; **$p < 0.01$; ***$p < 0.001$.

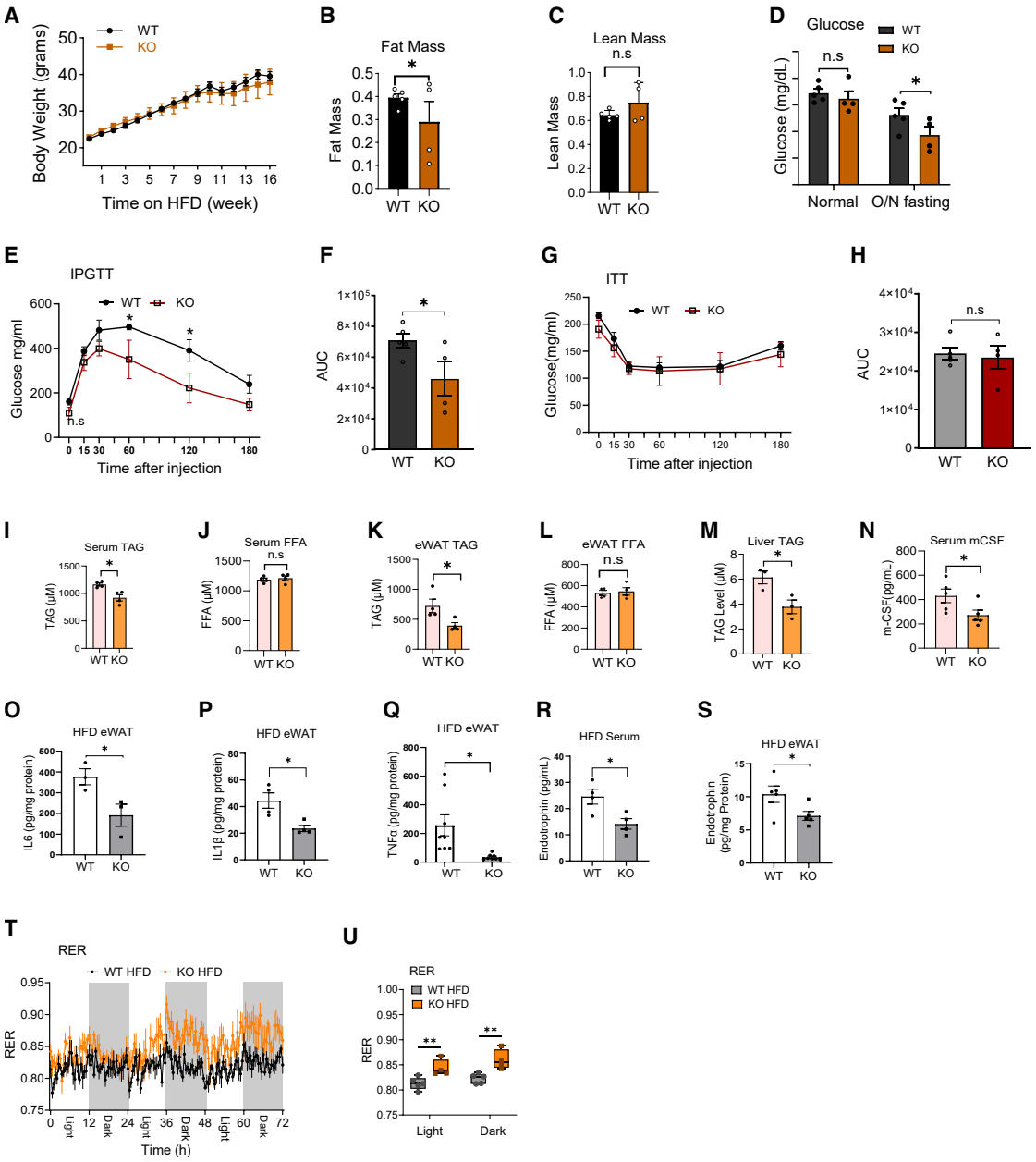

Figure 5. Myeloid MMP14 deficiency improves metabolic health under high-fat diet

(A) Body weight trajectories show that WT and LysM-Cre-*Mmp14* KO mice gain similar overall body weight during HFD feeding for 16 weeks. Data are presented as mean ± SEM.

(B and C) Body composition analysis demonstrated reduced fat mass and modestly increased lean mass in KO mice compared with WT controls (n = 4–5/group, Data are presented as mean ± SEM, Student's *t* test; n.s: no significance, $^*p < 0.05$.

(D) Circulating glucose levels do not differ between groups under normal feeding conditions, whereas overnight fasting circulating glucose levels are reduced in KO mice. (n = 4–5 per group), Data are presented as mean ± SEM, Student's *t* test; n.s: no significance, $^*p < 0.05$.

(E and F) Glucose tolerance test (GTT) shows improved circulating glucose levels following intraperitoneal (IP) glucose injection at different time points. *n* = 5 per group, Data are presented as mean ± SEM, Student's *t* test; $^*p < 0.05$).

(G and H) Insulin tolerance test (ITT) shows no significant differences between groups (*n* = 5 per group, mean ± SEM, Student's *t* test; n.s, no significance).

(I) Serum lipid measurements showing decreased circulating triglycerides in KO mice (*n* = 4/group, mean ± SEM, Student's *t* test; $^*p < 0.05$).

(J) Serum lipid measurements show no changes in circulating FFA in KO mice (*n* = 4/group, mean ± SEM, Student's *t* test, n.s, no significance).

(K) eWAT lipid measurements show decreased triglycerides in KO mice (*n* = 4/group, mean ± SEM, Student's *t* test, $^*p < 0.05$).

(L) eWAT lipid measurements show no change in total FFA in KO mice (*n* = 4/group, mean ± SEM, Student's *t* test, n.s, no significance).

(M) Liver lipid measurements show decreased triglycerides in KO mice (*n* = 4/group, mean ± SEM, Student's *t* test, $^*p < 0.05$).

(legend continued on next page)

depots confirmed a significant reduction in adipocyte hypertrophy in *Mmp14* KO mice (Figure 6B).

To determine whether these morphological changes were accompanied by alterations in lipid metabolic signaling, we next examined key regulators of lipid synthesis and breakdown by immunoblotting. In eWAT, immunoblot analysis showed increased phosphorylation of ACC and elevated expression of lipolytic enzymes, including ATGL, HSL, and carboxylesterase 1d (Ces1d), in *Mmp14* KO mice (Figures 6C and 6D). Expression of the lipid droplet-associated protein perilipin 1 (Plin1) was not significantly altered (Figures 6C and 6D).

Liver tissue was assessed to determine whether similar lipid metabolic remodeling occurred. Immunoblot analysis revealed increased expression of ATGL, HSL, and Ces1d in livers from *Mmp14* KO mice, together with an elevated *p*-ACC/ACC ratio, indicating altered hepatic lipid metabolic signaling (Figures 6E–6H). In parallel, levels of apolipoprotein B100 (ApoB100), a protein involved in hepatic lipid packaging and export, were reduced in *Mmp14* KO livers (Figures 6I and 6J). Because *Mmp14* KO mice showed altered substrate utilization and a trend toward increased energy expenditure, we next assessed whether thermogenic signaling in BAT was altered. Immunoblot analysis showed increased phosphorylation of protein kinase A (PKA) substrates in BAT from *Mmp14* KO mice (Figures 6K and 6L). In addition, expression of the thermogenic protein uncoupling protein 1 (UCP1) was increased in BAT from *Mmp14* KO mice, as assessed by immunofluorescence staining (Figure 6M) and confirmed by immunoblot analysis (Figures 6N and 6O).

Together, these data demonstrate coordinated lipid metabolic remodeling across WAT, liver, and BAT in *Mmp14* KO mice, characterized by reduced lipid storage, enhanced lipolytic signaling, and increased thermogenic UCP1 levels.

Myeloid Mmp14 deletion attenuates fibrosis and inflammatory immune remodeling

Given the established roles of macrophages in driving extracellular matrix remodeling and immune cell recruitment during obesity,[11–13,44,59] we next asked whether myeloid deletion of *Mmp14* alters fibrotic remodeling and immune cell composition in adipose tissue and liver under HFD feeding. To address this, histological, molecular, and immunophenotyping analyses were performed in metabolic tissues from WT and *Mmp14* KO mice. We first assessed tissue fibrosis by Masson's trichrome staining. In sWAT, collagen deposition was reduced in *Mmp14* KO mice compared with WT controls (Figure 7A). A similar reduction in collagen accumulation was observed in eWAT from *Mmp14* KO mice (Figure 7B). In contrast, liver sections showed only modest differences in collagen deposition between genotypes (Figure 7C), indicating that myeloid *Mmp14* deletion preferentially affects fibrotic remodeling in adipose tissue.

Because macrophage clustering around stressed adipocytes is a hallmark of adipose tissue inflammation,[60,61] we next examined macrophage accumulation within eWAT. Co-immunofluorescent staining for Mac2 (macrophage marker) and Plin1 (lipid droplet marker) revealed prominent crown-like macrophage structures in WT eWAT, whereas these structures were markedly reduced in *Mmp14* KO mice (Figures 7D and 7E). To determine whether macrophage accumulation was also altered in the liver, Mac2 immunostaining was performed. Macrophage-positive areas were reduced in livers from *Mmp14* KO mice compared with WT controls (Figures 7F and 7G).

We examined whether changes in fibrotic and cellular remodeling were accompanied by alterations in ECM-derived inflammatory mediators. Immunoblot analysis showed reduced levels of endotrophin in eWAT from *Mmp14* KO mice compared with WT controls (Figure 7H). Quantification confirmed a significant decrease in endotrophin levels in *Mmp14* KO eWAT (Figure 7I).

To assess downstream inflammatory signaling within tissues, expression of pro-inflammatory cytokines was examined by immunoblotting. In eWAT, levels of TNFα, IL-1β, and IL-6, except for NF-κB, were reduced *in Mmp14 KO* mice (Figures 7J and 7K). These findings are consistent with our previous observations of secreted factors in adipose tissue (Figures 5O–5Q). Similar reductions in inflammatory cytokine expression were observed in liver tissue from Mmp14 KO mice. Moreover, NF-κB expression was significantly decreased (Figures 7L and 7M).

To further define how myeloid *Mmp14* deletion affects immune cell composition within adipose tissue, SVFs were isolated from eWAT and analyzed by flow cytometry. Representative flow cytometry plots showed a significantly higher proportion of M1-like macrophages ($F4/80^+CD11c^+$) in eWAT from WT mice. In contrast, *Mmp14* KO mice showed no significant differences in the proportions of M1-like ($F4/80^+CD11c^+$) and M2-like ($F4/80^+CD206^+$) macrophages. Moreover, when compared with WT, *Mmp14* KO mice showed significantly less M1-like macrophages (Figures 7N and 7O; Figure S6A).

$TREM2^+$ macrophages have been linked to lipid-associated macrophages and are generally considered to exhibit a more M2-like, anti-inflammatory phenotype.[62,63] To further determine whether myeloid Mmp14 deletion affects $TREM2^+$ macrophage populations, we performed flow cytometry using the same SVF samples. Compared with WT mice, Mmp14 KO mice showed an increased proportion of $TREM2^+$ cells within the total macrophage population ($F4/80^+TREM2^+$), suggesting that MMP14

(N) Circulating inflammatory cytokines (e.g., *m*-CSF) are reduced in KO mice, indicating lower systemic inflammation (n = 5/group, mean ± SEM, Student's t test,*$p < 0.05$).
(O–Q) ELISA measurements of IL-6, IL-1β, and TNFα levels in eWAT from HFD-fed WT and *Mmp14* KO mice. Data are presented as mean ± SEM (n = 4–5 per group). Statistical significance was determined by Student's t test; *$p < 0.05$.
(R) ELISA measurement of endotrophin level in serum from HFD-fed WT and *Mmp14* KO mice. Data are presented as mean ± SEM (n = 4–5 per group). Statistical significance was determined by Student's t test; *$p < 0.05$.
(S) ELISA measurement of endotrophin level in eWAT from HFD-fed WT and *Mmp14* KO mice. Data are presented as mean ± SEM (n = 4–5 per group). Statistical significance was determined by Student's t test; *$p < 0.05$.
(T and U) Respiratory exchange ratio (RER) analyses show a shift toward greater fatty acid oxidation in KO mice. (n = 4–5 per group, mean ± SEM, one-way ANOVA followed by Fisher's post hoc analysis, **$p < 0.01$).

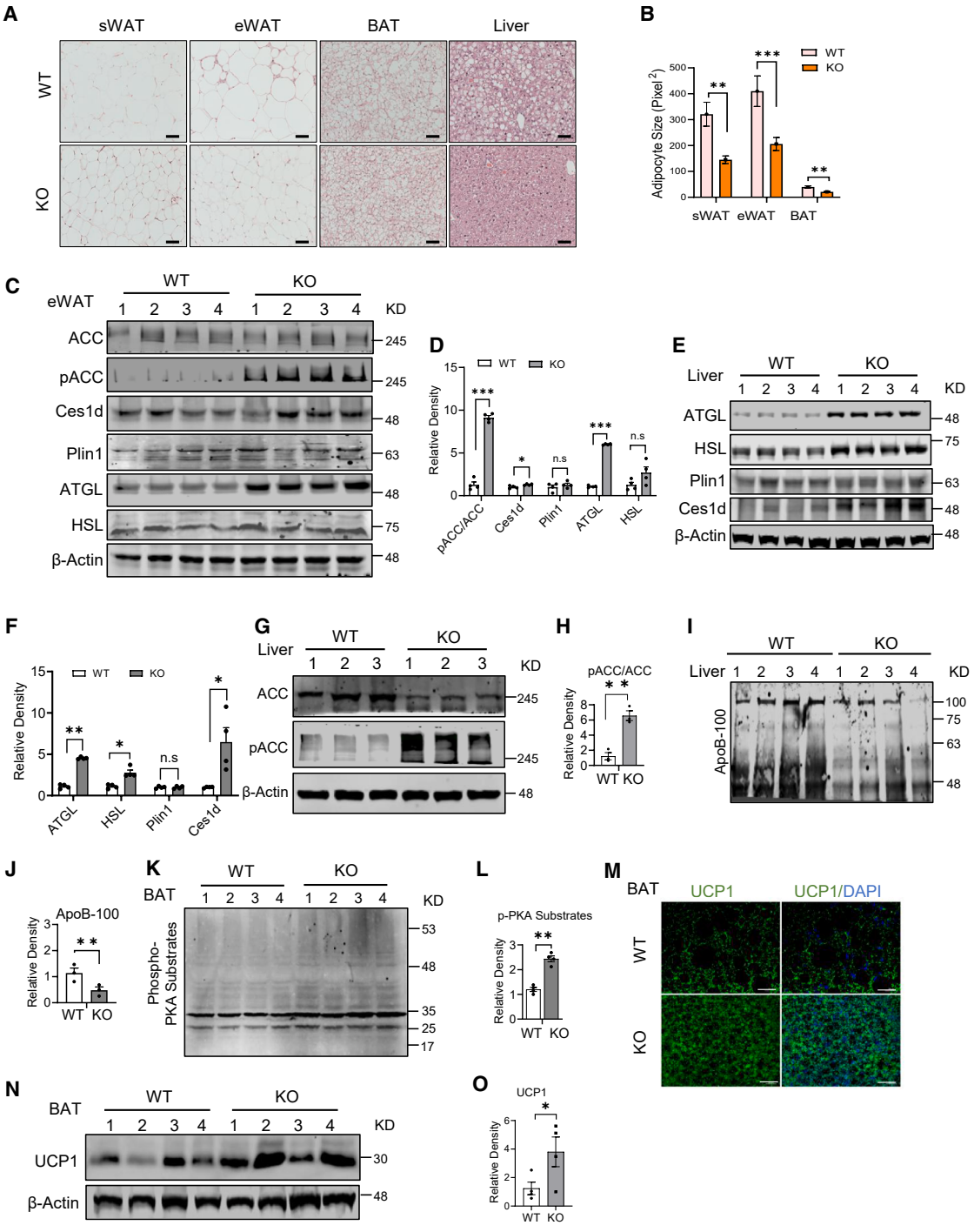

Figure 6. Myeloid-specific MMP14 deletion reprograms systemic lipid metabolism under HFD feeding

(A) H&E staining of sWAT, eWAT, BAT, and liver shows reduced adipocyte hypertrophy and attenuated hepatic lipid accumulation in MMP14 KO mice. Scale bar: 10 μm.

(B) Quantification of adipocyte size in the indicated adipose depots using ImageJ. A total of 16 areas of adipocytes were analyzed per group. Data of mean ± SEM were analyzed using Student's *t* test; $^{**}p < 0.01$, $^{***}p < 0.001$.

(C) Western blot analysis of lipogenic and lipolytic proteins, including ACC and *p*-ACC, Ces1d, Plin1, ATGL, and HSL, in eWAT from KO and WT mice following 16 weeks of HFD feeding.

(D) Quantification of band intensities in C demonstrates an increased *p*-ACC/ACC ratio and elevated levels of lipolytic proteins, including ATGL, HSL, and Ces1d, whereas Plin1 shows no significant change ($n = 4$/group). mean ± SEM, Student's *t* test, n.s, no significance, $^{*}p < 0.05$; $^{***}p < 0.001$.

(legend continued on next page)

deficiency promotes a lipid-associated macrophage phenotype (Figures 7P–7Q; Figure S6B).

This finding was further supported by confocal imaging of immunofluorescent staining for F4/80 (red) and TREM2 (green) in eWAT from HFD-fed WT and *Mmp14* KO mice. Although total macrophage numbers were reduced in Mmp14 KO eWAT, TREM2$^+$ staining signals were stronger (Figure 6C).

To confirm that endogenous macrophages exhibit similar properties, we further characterized macrophages directly isolated from the eWAT of HFD-fed WT and *Mmp14* KO mice. Macrophages from *Mmp14 KO* mice showed dramatically reduced endotrophin levels (Figures 7A and 7B). They also contained significantly lower levels of pro-inflammatory factors, including NF-κB, TNFα, IL-6, and IL-1β (Figures S7C and 7D). Furthermore, these macrophages exhibited reduced total ACC levels and increased levels of ATGL, HSL, and Ces1d (Figures S7E and 7F). Together, these changes are consistent with those observed in BMDMs and Raw264.7 cells, supporting the reproducibility of these findings across different macrophage sources.

We examined T cell populations within the same SVF samples. Flow cytometric analysis revealed a reduced proportion of CD8$^+$ T cells in eWAT from *Mmp14* KO, but not from WT mice (Figures 7R and 7S; Figure S6D). In contrast, the proportion of CD4$^+$ T cells was not significantly different between genotypes (Figures 7R and 7S).

Finally, total immune cell abundance was assessed. Quantification of total macrophages (F4/80$^+$) and total T cells (CD3$^+$) demonstrated an overall reduction in immune cell accumulation in eWAT from *Mmp14* KO mice compared with WT controls (Figure 7T). These data indicate that myeloid *Mmp14* deletion selectively reduces inflammatory immune cell populations within adipose tissue.

Schematic summary of the working model

A schematic overview of the experimental findings is shown in Figure 7U. The schematic illustrates the relationships observed between MMP14 expression in macrophages, endotrophin levels, inflammatory signaling, macrophage lipid accumulation, and tissue-level metabolic outcomes under HFD conditions. In the absence of MMP14, the schematic depicts reduced endotrophin production, lower inflammatory marker expression, increased macrophage lipolytic activity, decreased immune cell accumulation, reduced tissue fibrosis, and altered systemic metabolic parameters observed in *Mmp14* KO mice during HFD feeding.

DISCUSSION

Macrophage MMP14 as a regulator of immunometabolic remodeling in obesity

Obesity is accompanied by chronic low-grade inflammation, extensive ECM remodeling, and profound alterations in lipid metabolism within adipose tissue and liver. Macrophages are central to each of these processes and act as integrators of immune, stromal, and metabolic signals.[5,8,61,64] While the contribution of macrophages to inflammatory cytokine production and insulin resistance has been well established, considerably less is known about how macrophages respond to and interpret changes in the ECM during obesity.[12] In particular, the molecular mechanisms that connect ECM remodeling to macrophage lipid metabolism and whole-body energy balance have remained unclear. In this study, we identify macrophage MMP14 as a regulator that links ECM proteolysis to inflammatory activation and lipid metabolic remodeling in obesity. Our data indicate that MMP14 affects multiple aspects of macrophage biology, ranging from differentiation and functional maturation to inflammatory signaling and lipid handling. Importantly, these macrophage-intrinsic effects extend beyond the local tissue environment and are associated with changes in immune cell composition, lipid distribution across tissues, and systemic metabolic outcomes under high-fat diet conditions. These findings suggest that macrophage MMP14 functions as more than a matrix-remodeling enzyme. Instead, it acts as a molecular conduit through which structural changes in obese tissues are translated into immunometabolic dysfunction at the organismal level. MMP14 showed a transient increase followed by a decline during BMDM induction. Notably, its expression on day 6 was lower than on day 2, suggesting that MMP14 may regulate macrophage differentiation through a more complex mechanism.

Of note, we did not include lean mouse cohorts in this study because, under physiological lean conditions, metabolic tissues are largely devoid of inflammatory or metabolically activated macrophage populations. In this context, macrophages remain in a relatively quiescent state and do not exhibit the lipid-handling or activation phenotypes observed during metabolic stress. Consistent with this, macrophage-specific MMP14

(E) Western blot analysis of lipogenic Ces1d, Plin1, ATGL, and HSL, in the liver from KO and WT mice following 16 weeks of HFD feeding.
(F) Quantification of band intensities in D demonstrates elevated levels of lipolytic proteins, including ATGL, HSL, and Ces1d, whereas Plin1 shows no significant change (n = 4/group), mean ± SEM, Student's t test, n.s, no significance; *$p < 0.05$; **$p < 0.01$.
(G) Western blot analysis on ACC (p-ACC) in the liver of KO and WT mice following 16 weeks of HFD feeding.
(H) Quantification of band intensities in G demonstrates the increased ratio of p-ACC/ACC (n = 3 per group), mean ± SEM, Student's t test, **$p < 0.01$.
(I) Western Blot analysis on ApoB-100 in the liver from KO and WT mice following 16 weeks of HFD feeding.
(J) Quantification of band intensities in I demonstrates the reduced levels of ApoB −100 in the liver of the KO mice (n = 4/group, mean ± SEM, Student's t test, **$p < 0.01$).
(K) Western blot analysis on phosphorylated substrates by PKA in the BAT from KO and WT mice following 16 weeks of HFD feeding.
(L) Quantification of band intensities in K demonstrates the elevated levels of total phosphorylated substrates of PKA in the BAT of the KO mice (n = 4/group), mean ± SEM, Student's t test, **$p < 0.01$.
(M) Immunofluorescent staining of BAT using a specific α-UCP1 antibody shows increased UCP1 levels in BAT from KO mice. Cell nuclei were counterstained with DAPI. Scale bar: 25 μm.
(N) Western blot analysis on UCP1 protein levels in the BAT from KO and WT mice following 16 weeks of HFD feeding. β-Actin is the loading control.
(O) Quantification of band intensities in N demonstrates elevated levels of UCP1 in the BAT of the KO mice (n = 4/group), mean ± SEM, Student's t test, *$p < 0.05$.

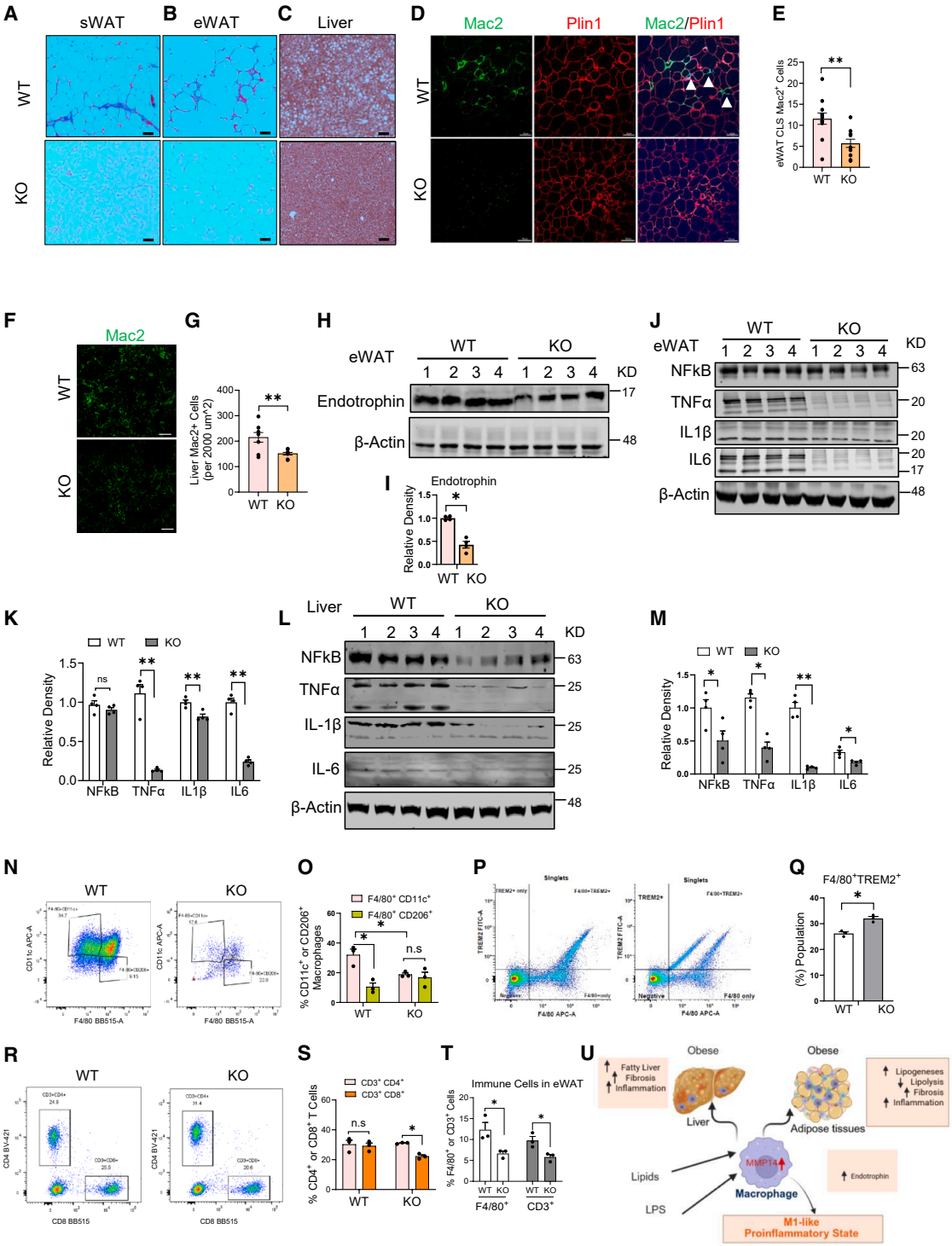

Figure 7. Reduced fibrosis, macrophage accumulation, and inflammation signaling in adipose tissue and liver of myeloid-specific MMP14 KO mice under HFD

(A–C) Masson's trichrome staining of sWAT(A), eWAT (B), and liver (C) from WT and KO mice shows reduced fibrosis in KO mice after 16 weeks of HFD feeding. Scale bar: 50 μm.

(D) Co-immunofluorescent staining of Mac2 and Plin1 in eWAT from WT and KO mice after 16 weeks of HFD feeding. White arrows in the WT merged images indicate crown-like structures formed by macrophage accumulation in obese adipose tissue, which are markedly reduced in KO mice. Scale bar: 100 μm.

(legend continued on next page)

deletion in lean mice did not produce any detectable phenotype, likely because MMP14-dependent functions are not engaged in unstimulated, healthy tissues (unpublished observations). Therefore, lean conditions are not suitable for interrogating the role of macrophage MMP14 in metabolic regulation.

MMP14 contributes to macrophage differentiation and functional capacity

Most previous studies have viewed macrophage MMP14 primarily as a pericellular collagenase that enables migration through dense fibrillar matrices when protease-independent motility is insufficient. Over time, this view has expanded from MMP14 as a simple, constitutively active surface protease to a broader role in three-dimensional matrix remodeling, macrophage survival, and cellular adaptation to complex tissue environments.[21,65–67] These functions are particularly relevant in fibrotic and tumor settings, where macrophages must navigate highly cross-linked collagen networks to infiltrate and persist within tissues.[22,31] Consistent with this framework, MMP14 has been implicated in collagen remodeling and inflammatory pathology in multiple disease contexts, including atherosclerosis, inflammatory arthritis, lung injury, and cancer.[27,28,67–70]

Our results substantially expand this framework. We show that MMP14 expression is dynamically induced during monocyte-to-macrophage differentiation and further elevated in macrophages from obese mice, suggesting a role early in macrophage development. Inhibition or genetic deletion of MMP14 impaired macrophage differentiation, proliferation, migration, and phagocytic capacity, indicating that MMP14 supports multiple aspects of macrophage functional competence. These defects cannot be explained solely by impaired migration, as they include reduced proliferative capacity and diminished phagocytosis. Together, these findings suggest that MMP14 contributes to macrophage maturation and responsiveness, potentially by shaping pericellular ECM interactions, signaling receptor availability, or access to matrix-bound ligands. In the context of obese adipose tissue, where macrophages are exposed to both lipid overload and progressive fibrosis, this broader role for MMP14 may be critical for sustaining macrophage activation and persistence.[12,42,44]

Macrophages as an MMP14-dependent source of endotrophin in obesity

Endotrophin, a cleavage product of the collagen VI α3 chain, was originally identified as an adipocyte-derived matrikine that promotes adipose tissue fibrosis, inflammation, angiogenesis, and systemic insulin resistance.[35,71] In this adipocyte-centric model, endotrophin is viewed primarily as a paracrine signal that shapes the fibrotic and inflammatory microenvironment of obese adipose tissue by recruiting immune cells and amplifying inflammatory signaling.[35,71,72] Subsequent studies established adipose-derived endotrophin as a key mediator linking ECM remodeling to metabolic dysfunction and identified MMP14 as the predominant protease responsible for endotrophin generation.[42] Notably, endotrophin promotes pro-inflammatory macrophage polarization in obese adipose tissue and *in vitro*.[57] Both

(E) Quantification of Mac2-positive cells in the crown-like structures in D for WT and KO eWAT (Representative of 10 fields. mean ± SEM, Student's *t* test; $^{**}p < 0.01$).
(F) Immunofluorescent staining of Mac2 in the liver from WT and KO mice after 16 weeks of HFD feeding. Scale bar: 100 μm.
(G) Quantification of Mac2-positive staining in F (representative of 8–9 fields; mean ± SEM, Student's *t* test, $^{**}p < 0.01$).
(H) Western blot analysis of endotrophin levels in eWAT from WT and KO mice. β-Actin serves as the loading control.
(I) Quantification of band intensities in H shows elevated endotrophin levels in WT eWAT, which are significantly reduced in KO eWAT ($n = 4$ per group); mean ± SEM, Student's *t* test, $^{*}p < 0.05$.
(J) Western blot analysis of pro-inflammatory factors, including NF-κB, TNF-α, IL-1β, and IL-6, in eWAT from WT and KO mice. β-Actin serves as the loading control.
(K) Quantification of band intensities in J shows slightly reduced total NF-κB levels, whereas TNF-α, IL-1β, and IL-6 levels are significantly reduced in KO eWAT ($n = 4$/group; mean ± SEM, Student's *t* test, n.s: not significant, $^{*}p < 0.05$, $^{**}p < 0.01$).
(L) Western blot analysis of pro-inflammatory factors, including NF-κB, TNF-α, IL-1β, and IL-6, in the liver of HFD-fed WT and KO mice. β-Actin serves as the loading control.
(M) Quantification of band intensities in L demonstrates significant reductions in NF-κB, TNF-α, IL-1β, and IL-6 in KO livers ($n = 4$ per group; mean ± SEM, Student's *t* test, $^{*}p < 0.05$; $^{**}p < 0.01$).
(N) Flow cytometric analysis of macrophage populations, including $F4/80^{+}CD11c^{+}$ and $F4/80^{+}CD206^{+}$ cells, in the SVF isolated from eWAT of the HFD-fed WT and KO mice.
(O) Quantification of M1-like ($F4/80^{+}CD11c^{+}$) and M2-like ($F4/80^{+}CD206^{+}$) macrophage populations in the SVF shown in N. ($n = 3$ per group, mean ± SEM, Student's *t* test, n.s: no significance; $^{*}p < 0.05$).
(P) Flow cytometric analysis of $F4/80^{+}TREM2^{+}$ macrophage populations, in the SVF isolated from eWAT of the HFD-fed WT and KO mice.
(Q) Quantification of $F4/80^{+}TREM2^{+}$ macrophage populations in SVF shown in P. ($n = 3$ per group; mean ± SEM, Student's *t* test, $^{*}p < 0.05$).
(R) Flow cytometric analysis of T cell populations, including $CD3^{+}CD4^{+}$ and $CD3^{+}CD8^{+}$ cells, in the SVF isolated from eWAT of the HFD-fed WT and KO mice.
(S) Quantification of $CD3^{+}CD4^{+}$ and $CD3^{+}CD8^{+}$ T cell populations in SVF shown in R. ($n = 3$ per group; mean ± SEM, Student's *t* test, n.s: no significance; $^{*}p < 0.05$).
(T) Quantification of $F4/80^{+}$ macrophage population and ($CD3^{+}$ T cell population in total SVF by flow cytometry shows reduced macrophage and T cell abundance in *Mmp14* KO eWAT. $n = 3$ per group; mean ± SEM, Student's *t* test, $^{*}p < 0.05$.
(U) A schematic illustration generated using Bio-Render depicting the role of macrophage MMP14 in response to lipid and LPS stimulation. Inflammatory (LPS) and lipid cues (OA, PA, oxLDL, and obese adipose-derived factors) induce MMP14 expression in macrophages, promoting TLR4-NFκB signaling, endotrophin production, and pro-inflammatory cytokine secretion (TNFα, IL-1β, and IL-6). Concurrently, MMP14 enhances lipid uptake, storage, and lipid droplet formation, driving macrophage inflammatory polarization and contributing to adipose and hepatic inflammation, fibrosis, and metabolic impairment. In contrast, inhibition or loss of MMP14 suppresses inflammatory signaling and endotrophin production, reduces TAG accumulation, enhances lipolysis, and improves tissue lipid handling and systemic metabolic outcomes.

endogenous and secreted endotrophin have been shown to exert profound fibrotic and pro-inflammatory effects by activating distinct signaling pathways.[35,40,57,58] Here, our findings revise and extend this paradigm by identifying macrophages as an additional, functionally relevant source of endotrophin. We show that macrophages produce endotrophin in response to adipose-derived and inflammatory stimuli and that this process depends on MMP14 activity. Importantly, restoration of endotrophin rescued pro-inflammatory cytokine production in MMP14-inhibited or *Mmp14*-deficient macrophages, demonstrating that macrophage-derived endotrophin directly contributes to macrophage inflammatory activation. These results suggest that endotrophin does not act exclusively as an adipocyte-to-macrophage signal. Instead, macrophages themselves can generate endotrophin, establishing an autocrine and paracrine feedback loop that reinforces inflammation. In fibrotic environments where macrophages are embedded within collagen-rich ECM, such a mechanism may be particularly effective at sustaining local inflammatory responses.

Endotrophin and macrophage lipid metabolic programming

Beyond its inflammatory functions, endotrophin has also been implicated in lipid metabolic regulation.[35,39] Prior studies have reported that endotrophin alone, or together with its parental collagen VI, suppresses lipolysis and promotes lipid accumulation in non-macrophage cell types, including adipocytes.[57,73] These observations raised the possibility that endotrophin contributes more broadly to lipid metabolic dysfunction during obesity, although its role within immune cells had not been directly examined.

Our data extend this concept by defining a macrophage-intrinsic metabolic phenotype associated with MMP14 activity. Loss or inhibition of MMP14 reduced lipid accumulation and enhanced lipolysis in macrophages across multiple lipid-loading contexts, including FFAs, oxidized LDL, and adipose tissue-derived conditioned media. These changes were accompanied by increased expression of lipolytic enzymes and enhanced ACC phosphorylation, consistent with a shift toward a more lipolytic metabolic state. Together, these findings indicate that ECM proteolysis influences macrophage lipid handling in a manner that is partially independent of classical inflammatory signaling.

Macrophage MMP14 regulates metabolic crosstalk with neighboring cells

Macrophages influence tissue metabolism through several mechanisms, including cytokine secretion, lipid scavenging, and metabolic signaling to neighboring cells.[9,62,74,75] In obese metabolic tissues, these interactions are particularly important because macrophages reside in close proximity to adipocytes and hepatocytes and are continuously exposed to excess nutrients, lipids, and inflammatory cues.[8–10,47,53,55,56,62,76,77] As a result, macrophage-derived signals can have outsized effects on tissue-level metabolic homeostasis. Consistent with this concept, we found that conditioned media from MMP14-inhibited or *Mmp14*-deficient macrophages reduced lipid accumulation in recipient cells. These findings suggest that macrophage MMP14 controls paracrine signals that shape lipid handling beyond the macrophage itself. Such signals likely include a combination of inflammatory mediators, lipid-derived metabolites, and ECM-associated factors. By regulating both inflammatory output and lipid metabolic cues, macrophage MMP14 may coordinate local tissue responses to nutrient excess and influence lipid flux across cell types. This provides a mechanism through which macrophage-intrinsic ECM remodeling can affect broader metabolic remodeling within obese tissues.

MMP14 influences immune remodeling in obese tissues

In addition to metabolic effects, myeloid Mmp14 deletion led to marked changes in immune cell composition within obese tissues. Knockout mice exhibited reduced accumulation of inflammatory macrophages and $CD8^+$ T cells in adipose tissue, while M2-like macrophages and $CD4^+$ T cells were largely unchanged. This pattern suggests a selective attenuation of inflammatory immune circuits rather than a generalized suppression of immune responses.

Previous studies have shown that $CD8^+$ T cells promote macrophage recruitment and adipose inflammation during obesity.[46] Our data suggest that macrophage MMP14-dependent programs contribute to sustaining this inflammatory immune environment, potentially through endotrophin-mediated ECM signaling and cytokine production. By disrupting this axis, *Mmp14* deletion attenuates both macrophage activation and secondary immune cell recruitment. This likely contributes to the reduced fibrosis and inflammation observed in metabolic tissues and reinforces the idea that ECM remodeling and immune remodeling are tightly linked processes in obesity.

The increase in $TREM2^+$ macrophages in eWAT from HFD-fed myeloid *Mmp14* KO mice suggests that loss of MMP14 not only reduces inflammatory macrophage accumulation but also shifts macrophage identity toward a lipid-associated, less inflammatory state.[62,63,78] This finding is consistent with the reduced adipose cytokine levels, endotrophin production, crown-like structures, fibrosis, and $CD8^+$ T cell accumulation observed in *Mmp14* KO mice, as well as the enhanced lipolytic markers in isolated adipose tissue macrophages. However, whether $TREM2^+$ macrophages directly mediate these metabolic benefits or arise secondarily from the improved tissue environment remains to be determined. Future studies using TREM2 loss-of-function approaches will be needed to define its causal contribution.

Systemic metabolic effects of myeloid MMP14 deletion

The *in vivo* phenotypes observed in myeloid-specific *Mmp14* knockout mice underscore the physiological relevance of macrophage MMP14 in metabolic disease. Despite similar weight gain during high-fat feeding, knockout mice exhibited improved glucose tolerance, reduced dyslipidemia, diminished hepatic steatosis, and lower circulating inflammatory markers. These improvements indicate that macrophage MMP14 contributes to metabolic dysfunction independently of effects on overall adiposity.

These metabolic changes were accompanied by an increased RER, and activation of brown adipose tissue thermogenic programs. Notably, these systemic effects resemble phenotypes

reported in endotrophin loss-of-function models, which also show improved metabolic health without major changes in body weight.[35] Our findings thus identify macrophage MMP14 as an upstream regulator that integrates endotrophin production with macrophage metabolic programming and systemic energy balance. This suggests that macrophage-derived ECM remodeling signals are sufficient to influence organismal metabolism during obesity.

Limitations of the study

Several limitations should be noted. LysM-Cre–mediated deletion targets multiple myeloid populations, including monocytes and neutrophils, and therefore does not isolate macrophage-specific effects *in vivo*. In addition, resident and recruited macrophages in liver, WAT and BAT are heterogeneous and are not fully recapitulated by *in vitro* BMDMs or Raw264.7 cells.[79] These models were used to define macrophage-intrinsic responses to specific lipid and inflammatory stimuli, not to claim full phenotypic equivalence with *in vivo* populations. Our aim was to link *in vivo* phenotypes to macrophage-intrinsic programs identified *in vitro*, while acknowledging the complexity of obesity-associated macrophage biology. Although the *in vitro* data support a macrophage-intrinsic role for MMP14, more selective genetic models will be needed to establish cell-type specificity *in vivo*.

Endotrophin is likely a contributing mediator rather than the sole driver of MMP14-dependent inflammatory activation. *In vitro* rescue experiments show that endotrophin is sufficient to restore inflammatory signaling in MMP14-inhibited or knockout macrophages. *In vivo*, reduced endotrophin levels in eWAT parallel decreases in inflammation and fibrosis. Together, these findings suggest that endotrophin functions within a broader MMP14-dependent signaling network. Future studies should determine whether MMP14 directly cleaves collagen VI in macrophages or acts through intermediary proteases. Further work is also needed to identify the macrophage-derived factors that mediate metabolic remodeling in neighboring cells and to determine how these signals integrate with systemic metabolic regulation. Addressing these questions will provide deeper insight into how ECM remodeling, immune activation, and metabolism are coordinated during obesity.

RESOURCE AVAILABILITY

Lead contact

Further information and requests for resources and reagents should be directed to and will be fulfilled by the lead contact, Kai Sun (kai.sun@uth.tmc.edu).

Materials availability

All unique/stable reagents generated in this study are available from the lead contact with a completed materials transfer agreement (MTA).

Data and code availability

- Data: RNA-seq datasets generated in this study have been deposited in the Gene Expression Omnibus (GEO) under accession number GSE335244 and are publicly accessible as of June 22, 2026. Publicly available GEO dataset GDS2429 was also analyzed as indicated in the manuscript.
- Code: No custom code was generated in this study. Software and algorithms used for data analysis, including Cal-R software, are listed in the key resources table.
- Other items: Any additional information required to reanalyze the data reported in this paper is available from the lead contact upon request.

ACKNOWLEDGMENTS

The authors thank Dr. Stephen J. Weiss (Division of Pulmonary and Critical Care Medicine, Department of Internal Medicine, University of Michigan, and the Life Sciences Institute) for generously providing the *Mmp14* $^{flox/flox}$ mouse line and for his valuable guidance throughout this project. We also thank our colleagues at the Center for Metabolic and Degenerative Diseases at UTHealth for technical support and helpful discussions. We are grateful to Dr. Zhengmei Mao and Dr. Travis Moore at the Microscopy Core of the Institute of Molecular Medicine for assistance with imaging and tissue processing. Fluorescence microscopy was performed at the Center for Advanced Microscopy, a Nikon Center of Excellence, at McGovern Medical School, UTHealth Houston (RRID: SCR_025962). We thank Dr. Ville Meretoja of the Flow Cytometry Core at the Institute of Molecular Medicine, UTHealth Houston, for his helpful input; and Dr. Haichao Wei at IMM for his help for RNA-seq data analysis. We also thank Dr. Yuxiang Sun and her laboratory at the Department of Nutrition at Texas A&M University for their critical technical supports. This work was supported by National Institutes of Health grants R01DK129815 and R01DK109001 (to K.S.), R01DK138018 (to S.H.), and NIGMS R35GM141089 (to X.G.). RNA sequencing was performed by the Cancer Genomics Core, supported by the UTHealth Cancer Prevention and Research Institute of Texas (CPRIT RP180734).

AUTHOR CONTRIBUTIONS

Conception, design, and supervision, K.S.; acquisition and analyses, L.J.S., F.E., F.G., E.L.L., B.R., M.E., I.M., K.E.-M., P.E.S., X.G., H.W., S.H., and K.S.; interpretation of data, P.E.S., H.W., S.H., and K.S.; project administration and funding acquisition, K.S., S.H., X.G. All authors edited, read and approved the final manuscript.

DECLARATION OF INTERESTS

All the authors declare no competing interests.

STAR★METHODS

Detailed methods are provided in the online version of this paper and include the following:

- KEY RESOURCES TABLE
- EXPERIMENTAL MODEL AND STUDY PARTICIPANT DETAILS
  - Animals
- METHOD DETAILS
  - Body composition and indirect calorimetry
  - Glucose tolerance and insulin tolerance tests
  - Serum biochemistry
  - Tissue processing and histology
  - Immunofluorescence staining of tissue sections
  - eWAT-conditioned medium preparation
  - Cell culture and treatments
  - *Isolation of Brewer Thioglycollate-elicited peritoneal macrophages*
  - eWAT-resident macrophage isolation
  - Bone marrow–derived macrophage (BMDM) differentiation and treatment
  - Lipid droplet staining
  - Migration assays
  - Phagocytosis assays
  - Flow cytometry
  - Western blotting
  - RNA sequencing

- Quantitative PCR
- Statistical analysis

SUPPLEMENTAL INFORMATION

Supplemental information can be found online at https://doi.org/10.1016/j.celrep.2026.117681.

Received: February 15, 2026
Revised: May 20, 2026
Accepted: June 24, 2026

REFERENCES

1. Alsabeeh, N., Chausse, B., Kakimoto, P.A., Kowaltowski, A.J., and Shirihai, O. (2018). Cell culture models of fatty acid overload: Problems and solutions. Biochim. Biophys. Acta. Mol. Cell Biol. Lipids *1863*, 143–151. https://doi.org/10.1016/j.bbalip.2017.11.006.
2. Fabbrini, E., Sullivan, S., and Klein, S. (2010). Obesity and nonalcoholic fatty liver disease: biochemical, metabolic, and clinical implications. Hepatology *51*, 679–689. https://doi.org/10.1002/hep.23280.
3. Sun, K., Li, X., and Scherer, P.E. (2023). Extracellular Matrix (ECM) and Fibrosis in Adipose Tissue: Overview and Perspectives. Compr. Physiol. *13*, 4387–4407. https://doi.org/10.1002/cphy.c220020.
4. Marchesini, G., Moscatiello, S., Di Domizio, S., and Forlani, G. (2008). Obesity-associated liver disease. J. Clin. Endocrinol. Metab. *93*, S74–S80. https://doi.org/10.1210/jc.2008-1399.
5. Hotamisligil, G.S., Shargill, N.S., and Spiegelman, B.M. (1993). Adipose expression of tumor necrosis factor-alpha: direct role in obesity-linked insulin resistance. Science *259*, 87–91. https://doi.org/10.1126/science.7678183.
6. Weisberg, S.P., McCann, D., Desai, M., Rosenbaum, M., Leibel, R.L., and Ferrante, A.W., Jr. (2003). Obesity is associated with macrophage accumulation in adipose tissue. J. Clin. Investig. *112*, 1796–1808. https://doi.org/10.1172/JCI19246.
7. Xu, H., Barnes, G.T., Yang, Q., Tan, G., Yang, D., Chou, C.J., Sole, J., Nichols, A., Ross, J.S., Tartaglia, L.A., and Chen, H. (2003). Chronic inflammation in fat plays a crucial role in the development of obesity-related insulin resistance. J. Clin. Investig. *112*, 1821–1830. https://doi.org/10.1172/JCI19451.
8. Olefsky, J.M., and Glass, C.K. (2010). Macrophages, inflammation, and insulin resistance. Annu. Rev. Physiol. *72*, 219–246. https://doi.org/10.1146/annurev-physiol-021909-135846.
9. Meng, W., Xiao, T., Liang, X., Wen, J., Peng, X., Wang, J., Zou, Y., Liu, J., Bialowas, C., Luo, H., et al. (2021). The miR-182-5p/FGF21/acetylcholine axis mediates the crosstalk between adipocytes and macrophages to promote beige fat thermogenesis. JCI Insight *6*, e150249. https://doi.org/10.1172/jci.insight.150249.
10. Karlmark, K.R., Weiskirchen, R., Zimmermann, H.W., Gassler, N., Ginhoux, F., Weber, C., Merad, M., Luedde, T., Trautwein, C., and Tacke, F. (2009). Hepatic recruitment of the inflammatory Gr1+ monocyte subset upon liver injury promotes hepatic fibrosis. Hepatology *50*, 261–274. https://doi.org/10.1002/hep.22950.
11. Heymann, F., Trautwein, C., and Tacke, F. (2009). Monocytes and macrophages as cellular targets in liver fibrosis. Inflamm. Allergy Drug Targets *8*, 307–318. https://doi.org/10.2174/187152809789352230.
12. Dahdah, N., Tercero-Alcázar, C., Malagón, M.M., Garcia-Roves, P.M., and Guzmán-Ruiz, R. (2024). Interrelation of adipose tissue macrophages and fibrosis in obesity. Biochem. Pharmacol. *225*, 116324. https://doi.org/10.1016/j.bcp.2024.116324.
13. Yao, J., Wu, D., and Qiu, Y. (2022). Adipose tissue macrophage in obesity-associated metabolic diseases. Front. Immunol. *13*, 977485. https://doi.org/10.3389/fimmu.2022.977485.
14. Rabhi, N., Desevin, K., Belkina, A.C., Tilston-Lunel, A., Varelas, X., Layne, M.D., and Farmer, S.R. (2022). Obesity-induced senescent macrophages activate a fibrotic transcriptional program in adipocyte progenitors. Life Sci. Alliance *5*, e202101286. https://doi.org/10.26508/lsa.202101286.
15. Kunz, H.E., Hart, C.R., Gries, K.J., Parvizi, M., Laurenti, M., Dalla Man, C., Moore, N., Zhang, X., Ryan, Z., Polley, E.C., et al. (2021). Adipose tissue macrophage populations and inflammation are associated with systemic inflammation and insulin resistance in obesity. Am. J. Physiol. Endocrinol. Metab. *321*, E105–E121. https://doi.org/10.1152/ajpendo.00070.2021.
16. de Almeida, L.G.N., Thode, H., Eslambolchi, Y., Chopra, S., Young, D., Gill, S., Devel, L., and Dufour, A. (2022). Matrix Metalloproteinases: From Molecular Mechanisms to Physiology, Pathophysiology, and Pharmacology. Pharmacol. Rev. *74*, 712–768. https://doi.org/10.1124/pharmrev.121.000349.
17. Seiki, M., Mori, H., Kajita, M., Uekita, T., and Itoh, Y. (2003). Membrane-type 1 matrix metalloproteinase and cell migration. Biochem. Soc. Symp. *70*, 253–262. https://doi.org/10.1042/bss0700253.
18. Takino, T., Miyamori, H., Watanabe, Y., Yoshioka, K., Seiki, M., and Sato, H. (2004). Membrane type 1 matrix metalloproteinase regulates collagen-dependent mitogen-activated protein/extracellular signal-related kinase activation and cell migration. Cancer Res. *64*, 1044–1049. https://doi.org/10.1158/0008-5472.can-03-1843.
19. Munshi, H.G., Wu, Y.I., Mukhopadhyay, S., Ottaviano, A.J., Sassano, A., Koblinski, J.E., Platanias, L.C., and Stack, M.S. (2004). Differential regulation of membrane type 1-matrix metalloproteinase activity by ERK 1/2- and p38 MAPK-modulated tissue inhibitor of metalloproteinases 2 expression controls transforming growth factor-beta1-induced pericellular collagenolysis. J. Biol. Chem. *279*, 39042–39050. https://doi.org/10.1074/jbc.M404958200.
20. Taylor, S.H., Yeung, C.Y.C., Kalson, N.S., Lu, Y., Zigrino, P., Starborg, T., Warwood, S., Holmes, D.F., Canty-Laird, E.G., Mauch, C., and Kadler, K.E. (2015). Matrix metalloproteinase 14 is required for fibrous tissue expansion. eLife *4*, e09345. https://doi.org/10.7554/eLife.09345.
21. Chun, T.H., Sabeh, F., Ota, I., Murphy, H., McDonagh, K.T., Holmbeck, K., Birkedal-Hansen, H., Allen, E.D., and Weiss, S.J. (2004). MT1-MMP-dependent neovessel formation within the confines of the three-dimensional extracellular matrix. J. Cell Biol. *167*, 757–767. https://doi.org/10.1083/jcb.200405001.
22. Sabeh, F., Ota, I., Holmbeck, K., Birkedal-Hansen, H., Soloway, P., Balbin, M., Lopez-Otin, C., Shapiro, S., Inada, M., Krane, S., et al. (2004). Tumor cell traffic through the extracellular matrix is controlled by the membrane-anchored collagenase MT1-MMP. J. Cell Biol. *167*, 769–781. https://doi.org/10.1083/jcb.200408028.
23. Apte, S.S., Fukai, N., Beier, D.R., and Olsen, B.R. (1997). The matrix metalloproteinase-14 (MMP-14) gene is structurally distinct from other MMP genes and is co-expressed with the TIMP-2 gene during mouse embryogenesis. J. Biol. Chem. *272*, 25511–25517. https://doi.org/10.1074/jbc.272.41.25511.
24. Xiong, W., Knispel, R., MacTaggart, J., Greiner, T.C., Weiss, S.J., and Baxter, B.T. (2009). Membrane-type 1 matrix metalloproteinase regulates macrophage-dependent elastolytic activity and aneurysm formation in vivo. J. Biol. Chem. *284*, 1765–1771. https://doi.org/10.1074/jbc.M806239200.
25. Shimizu-Hirota, R., Xiong, W., Baxter, B.T., Kunkel, S.L., Maillard, I., Chen, X.W., Sabeh, F., Liu, R., Li, X.Y., and Weiss, S.J. (2012). MT1-MMP regulates the PI3Kdelta.Mi-2/NuRD-dependent control of macrophage immune function. Genes Dev. *26*, 395–413. https://doi.org/10.1101/gad.178749.111.
26. Ray, B.K., Shakya, A., Turk, J.R., Apte, S.S., and Ray, A. (2004). Induction of the MMP-14 gene in macrophages of the atherosclerotic plaque: role of SAF-1 in the induction process. Circ. Res. *95*, 1082–1090. https://doi.org/10.1161/01.RES.0000150046.48115.80.
27. Gonzalo, P., Guadamillas, M.C., Hernández-Riquer, M.V., Pollán, A., Grande-García, A., Bartolomé, R.A., Vasanji, A., Ambrogio, C., Chiarle,

R., Teixidó, J., et al. (2010). MT1-MMP is required for myeloid cell fusion via regulation of Rac1 signaling. Dev. Cell *18*, 77–89. https://doi.org/10.1016/j.devcel.2009.11.012.

28. Schneider, F., Sukhova, G.K., Aikawa, M., Canner, J., Gerdes, N., Tang, S.M.T., Shi, G.P., Apte, S.S., and Libby, P. (2008). Matrix-metalloproteinase-14 deficiency in bone-marrow-derived cells promotes collagen accumulation in mouse atherosclerotic plaques. Circulation *117*, 931–939. https://doi.org/10.1161/CIRCULATIONAHA.107.707448.
29. Johnson, J.L., Jenkins, N.P., Huang, W.C., Di Gregoli, K., Sala-Newby, G.B., Scholtes, V.P.W., Moll, F.L., Pasterkamp, G., and Newby, A.C. (2014). Relationship of MMP-14 and TIMP-3 expression with macrophage activation and human atherosclerotic plaque vulnerability. Mediators Inflamm. *2014*, 276457. https://doi.org/10.1155/2014/276457.
30. Xia, X.D., Gill, G., Lin, H., Roth, D.M., Gu, H.m., Wang, X.j., Su, F.y., Alabi, A., Alexiou, M., Zhang, Z., et al. (2023). Global, but not chondrocyte-specific, MT1-MMP deficiency in adult mice causes inflammatory arthritis. Matrix Biol. *122*, 10–17. https://doi.org/10.1016/j.matbio.2023.08.003.
31. Feinberg, T.Y., Zheng, H., Liu, R., Wicha, M.S., Yu, S.M., and Weiss, S.J. (2018). Divergent Matrix-Remodeling Strategies Distinguish Developmental from Neoplastic Mammary Epithelial Cell Invasion Programs. Dev. Cell *47*, 145–160.e6. https://doi.org/10.1016/j.devcel.2018.08.025.
32. Szabova, L., Chrysovergis, K., Yamada, S.S., and Holmbeck, K. (2008). MT1-MMP is required for efficient tumor dissemination in experimental metastatic disease. Oncogene *27*, 3274–3281. https://doi.org/10.1038/sj.onc.1210982.
33. Solomonov, I., Kollet, O., and Sagi, I. (2025). Extracellular matrix and proteolysis: mechanisms driving irreversible changes and shaping cell behavior. FEBS J. febs.70292. https://doi.org/10.1111/febs.70292.
34. Smith, G.I., and Klein, S. (2025). Plasma endotrophin levels correlate with insulin resistance in people with obesity. J. Clin. Investig. *135*, e190577. https://doi.org/10.1172/JCI190577.
35. Sun, K., Park, J., Gupta, O.T., Holland, W.L., Auerbach, P., Zhang, N., Goncalves Marangoni, R., Nicoloro, S.M., Czech, M.P., Varga, J., et al. (2014). Endotrophin triggers adipose tissue fibrosis and metabolic dysfunction. Nat. Commun. *5*, 3485. https://doi.org/10.1038/ncomms4485.
36. Genovese, F., Karsdal, M., Devos, H., Bager, C., Nuñez, J., and Bayes-Genis, A. (2026). Endotrophin as a biomarker and mediator in cardiovascular-kidney-metabolic syndrome: current insights and remaining questions. American Journal of Physiology-Cell Physiology *330*, C409–C420. https://doi.org/10.1152/ajpcell.00769.2025.
37. Kim, D.S., Funcke, J.B., Chen, S., Min, K., Onodera, T., Kim, M., Lin, Q., Joung, C., Velasco, J., Virostek, M., et al. (2025). ETP-specific-knockout mice reveal endotrophin as a key regulator of kidney fibrosis in ischemia-reperfusion injury models. Exp. Mol. Med. *57*, 2475–2486. https://doi.org/10.1038/s12276-025-01567-1.
38. Eruzun, H., Avcıoğlu, U., Gören, İ., Ürkmez, Y., Kuçukdemirci, Ö., Zorlu, B., Isgandarov, E., Ustaoğlu, M., Ayyıldız, T., Yıldırım, B., and Bektaş, A. (2025). Circulating Endotrophin as a Biomarker of Fibrosis in Chronic Liver Diseases. Niger. J. Clin. Pract. *28*, 737–743. https://doi.org/10.4103/njcp.njcp_384_24.
39. Henriksen, K., Genovese, F., Reese-Petersen, A., Audoly, L.P., Sun, K., Karsdal, M.A., and Scherer, P.E. (2024). Endotrophin, a Key Marker and Driver for Fibroinflammatory Disease. Endocr. Rev. *45*, 361–378. https://doi.org/10.1210/endrev/bnad036.
40. Oh, J., Park, C., Kim, S., Kim, M., Kim, C.S., Jo, W., Park, S., Yi, G.S., and Park, J. (2023). High levels of intracellular endotrophin in adipocytes mediate COPII vesicle supplies to autophagosome to impair autophagic flux and contribute to systemic insulin resistance in obesity. Metabolism *145*, 155629. https://doi.org/10.1016/j.metabol.2023.155629.
41. Hagström, H., Bu, D., Nasr, P., Ekstedt, M., Hegmar, H., Kechagias, S., Zhang, N., An, Z., Stål, P., and Scherer, P.E. (2021). Serum levels of endotrophin are associated with nonalcoholic steatohepatitis. Scand. J. Gastroenterol. *56*, 437–442. https://doi.org/10.1080/00365521.2021.1879249.
42. Li, X., Zhao, Y., Chen, C., Yang, L., Lee, H.h., Wang, Z., Zhang, N., Kolonin, M.G., An, Z., Ge, X., et al. (2020). Critical Role of Matrix Metalloproteinase 14 in Adipose Tissue Remodeling during Obesity. Mol. Cell Biol. *40*, e00564-19. https://doi.org/10.1128/MCB.00564-19.
43. Sun, K., Kusminski, C.M., and Scherer, P.E. (2011). Adipose tissue remodeling and obesity. J. Clin. Investig. *121*, 2094–2101. https://doi.org/10.1172/JCI45887.
44. Kratz, M., Coats, B.R., Hisert, K.B., Hagman, D., Mutskov, V., Peris, E., Schoenfelt, K.Q., Kuzma, J.N., Larson, I., Billing, P.S., et al. (2014). Metabolic dysfunction drives a mechanistically distinct proinflammatory phenotype in adipose tissue macrophages. Cell Metab. *20*, 614–625. https://doi.org/10.1016/j.cmet.2014.08.010.
45. Kiran, S., Kumar, V., Murphy, E.A., Enos, R.T., and Singh, U.P. (2021). High Fat Diet-Induced CD8(+) T Cells in Adipose Tissue Mediate Macrophages to Sustain Low-Grade Chronic Inflammation. Front. Immunol. *12*, 680944. https://doi.org/10.3389/fimmu.2021.680944.
46. Nishimura, S., Manabe, I., Nagasaki, M., Eto, K., Yamashita, H., Ohsugi, M., Otsu, M., Hara, K., Ueki, K., Sugiura, S., et al. (2009). CD8+ effector T cells contribute to macrophage recruitment and adipose tissue inflammation in obesity. Nat. Med. *15*, 914–920. https://doi.org/10.1038/nm.1964.
47. Li, J., Li, Y., Zhou, X., Yang, S., Liu, D., Wen, H., Chen, X., Duan, C., Yu, M., Zhang, M., et al. (2025). Adipocytes orchestrate obesity-related chronic inflammation through beta2-microglobulin. Signal Transduct. Target. Ther. *10*, 394. https://doi.org/10.1038/s41392-025-02486-3.
48. Wang, Q., and Wu, H. (2018). T Cells in Adipose Tissue: Critical Players in Immunometabolism. Front. Immunol. *9*, 2509. https://doi.org/10.3389/fimmu.2018.02509.
49. Khan, I.M., Dai Perrard, X.Y., Perrard, J.L., Mansoori, A., Wayne Smith, C., Wu, H., and Ballantyne, C.M. (2014). Attenuated adipose tissue and skeletal muscle inflammation in obese mice with combined CD4+ and CD8+ T cell deficiency. Atherosclerosis *233*, 419–428. https://doi.org/10.1016/j.atherosclerosis.2014.01.011.
50. Remacle, A.G., Cieplak, P., Nam, D.H., Shiryaev, S.A., Ge, X., and Strongin, A.Y. (2017). Selective function-blocking monoclonal human antibody highlights the important role of membrane type-1 matrix metalloproteinase (MT1-MMP) in metastasis. Oncotarget *8*, 2781–2799. https://doi.org/10.18632/oncotarget.13157.
51. Bechor, S., Nachmias, D., Elia, N., Haim, Y., Vatarescu, M., Leikin-Frenkel, A., Gericke, M., Tarnovscki, T., Las, G., and Rudich, A. (2017). Adipose tissue conditioned media support macrophage lipid-droplet biogenesis by interfering with autophagic flux. Biochim. Biophys. Acta. Mol. Cell Biol. Lipids *1862*, 1001–1012. https://doi.org/10.1016/j.bbalip.2017.06.012.
52. Cory, G. (2011). Scratch-wound assay. Methods Mol. Biol. *769*, 25–30. https://doi.org/10.1007/978-1-61779-207-6_2.
53. Boutens, L., and Stienstra, R. (2016). Adipose tissue macrophages: going off track during obesity. Diabetologia *59*, 879–894. https://doi.org/10.1007/s00125-016-3904-9.
54. Su, T., He, Y., Wang, M., Zhou, H., Huang, Y., Ye, M., Guo, Q., Xiao, Y., Cai, G., Zhao, M., et al. (2024). Macrophage-Hepatocyte Circuits Mediated by Grancalcin Aggravate the Progression of Metabolic Dysfunction Associated Steatohepatitis. Adv. Sci. *11*, e2406500. https://doi.org/10.1002/advs.202406500.
55. Huh, J.Y., Park, Y.J., Ham, M., and Kim, J.B. (2014). Crosstalk between adipocytes and immune cells in adipose tissue inflammation and metabolic dysregulation in obesity. Mol. Cells *37*, 365–371. https://doi.org/10.14348/molcells.2014.0074.
56. Kim, D.M., Pan, Q., Liu, Z., Ai, W., Han, H.W., Banu, S.K., Tsai, R.Y., Wright, G.A., Guo, S., and Sun, Y. (2025). GHSR-Foxo1 Signaling in Macrophages Promotes Liver Fibrosis via Inflammatory Response and Hepatic

Stellate Cell Activation. Adv. Sci. (Weinh.) *12*, e04223. https://doi.org/10.1002/advs.202504223.

57. Zhao, Y., Gu, X., Zhang, N., Kolonin, M.G., An, Z., and Sun, K. (2016). Divergent functions of endotrophin on different cell populations in adipose tissue. Am. J. Physiol. Endocrinol. Metabol. *311*, E952–E963. https://doi.org/10.1152/ajpendo.00314.2016.

58. Kim, C.S., Jo, W., Yoo, J., Kim, M., An, J.P., Oh, W.K., and Park, J. (2026). Targeting COL6A3-C5 with nigericin suppresses endotrophin formation and enhances insulin sensitivity in obesity. Exp. Mol. Med. *58*, 768–781. https://doi.org/10.1038/s12276-026-01661-y.

59. Thomas, D., and Apovian, C. (2017). Macrophage functions in lean and obese adipose tissue. Metabolism *72*, 120–143. https://doi.org/10.1016/j.metabol.2017.04.005.

60. Coenen, K.R., Gruen, M.L., Chait, A., and Hasty, A.H. (2007). Diet-induced increases in adiposity, but not plasma lipids, promote macrophage infiltration into white adipose tissue. Diabetes *56*, 564–573. https://doi.org/10.2337/db06-1375.

61. Lumeng, C.N., Bodzin, J.L., and Saltiel, A.R. (2007). Obesity induces a phenotypic switch in adipose tissue macrophage polarization. J. Clin. Investig. *117*, 175–184. https://doi.org/10.1172/JCI29881.

62. Jaitin, D.A., Adlung, L., Thaiss, C.A., Weiner, A., Li, B., Descamps, H., Lundgren, P., Bleriot, C., Liu, Z., Deczkowska, A., et al. (2019). Lipid-Associated Macrophages Control Metabolic Homeostasis in a Trem2-Dependent Manner. Cell *178*, 686–698.e14. https://doi.org/10.1016/j.cell.2019.05.054.

63. Zhou, L., Lu, Y., Qiu, X., Chen, Z., Tang, Y., Meng, Z., Yan, C., Du, H., Li, S., and Lin, J.D. (2025). Lipid droplet efferocytosis attenuates proinflammatory signaling in macrophages via TREM2- and MS4A7-dependent mechanisms. Cell Rep. *44*, 115310. https://doi.org/10.1016/j.celrep.2025.115310.

64. Nance, S.A., Muir, L., and Lumeng, C. (2022). Adipose tissue macrophages: Regulators of adipose tissue immunometabolism during obesity. Mol. Metab. *66*, 101642. https://doi.org/10.1016/j.molmet.2022.101642.

65. Sabeh, F., Li, X.Y., Olson, A.W., Botvinick, E., Kurup, A., Gimenez, L.E., Cho, J.S., and Weiss, S.J. (2024). Mmp14-dependent remodeling of the pericellular-dermal collagen interface governs fibroblast survival. J. Cell Biol. *223*, e202312091. https://doi.org/10.1083/jcb.202312091.

66. Peck, B.D., Murach, K.A., Walton, R.G., Simmons, A.J., Long, D.E., Kosmac, K., Dungan, C.M., Kern, P.A., Bamman, M.M., and Peterson, C.A. (2022). A muscle cell-macrophage axis involving matrix metalloproteinase 14 facilitates extracellular matrix remodeling with mechanical loading. FASEB J. *36*, e22155. https://doi.org/10.1096/fj.202100182RR.

67. Peng, D., Li, J., Li, Y., Bai, L., Xiong, A., He, X., Li, X., Ran, Q., Zhang, L., Jiang, M., et al. (2024). MMP14(high) macrophages orchestrate progressive pulmonary fibrosis in SR-Ag-induced hypersensitivity pneumonitis. Pharmacol. Res. *200*, 107070. https://doi.org/10.1016/j.phrs.2024.107070.

68. Stawowczyk, M., Wellenstein, M.D., Lee, S.B., Yomtoubian, S., Durrans, A., Choi, H., Narula, N., Altorki, N.K., Gao, D., and Mittal, V. (2017). Matrix Metalloproteinase 14 promotes lung cancer by cleavage of Heparin-Binding EGF-like Growth Factor. Neoplasia *19*, 55–64. https://doi.org/10.1016/j.neo.2016.11.005.

69. Talmi-Frank, D., Altboum, Z., Solomonov, I., Udi, Y., Jaitin, D.A., Klepfish, M., David, E., Zhuravlev, A., Keren-Shaul, H., Winter, D.R., et al. (2016). Extracellular Matrix Proteolysis by MT1-MMP Contributes to Influenza-Related Tissue Damage and Mortality. Cell Host Microbe *20*, 458–470. https://doi.org/10.1016/j.chom.2016.09.005.

70. Zigrino, P., Brinckmann, J., Niehoff, A., Lu, Y., Giebeler, N., Eckes, B., Kadler, K.E., and Mauch, C. (2016). Fibroblast-Derived MMP-14 Regulates Collagen Homeostasis in Adult Skin. J. Invest. Dermatol. *136*, 1575–1583. https://doi.org/10.1016/j.jid.2016.03.036.

71. Park, J., and Scherer, P.E. (2012). Endotrophin - a novel factor linking obesity with aggressive tumor growth. Oncotarget *3*, 1487–1488. https://doi.org/10.18632/oncotarget.796.

72. Park, J., Morley, T.S., and Scherer, P.E. (2013). Inhibition of endotrophin, a cleavage product of collagen VI, confers cisplatin sensitivity to tumours. EMBO Mol. Med. *5*, 935–948. https://doi.org/10.1002/emmm.201202006.

73. Oh, J., Kim, C.S., Kim, M., Jo, W., Sung, Y.H., and Park, J. (2021). Type VI collagen and its cleavage product, endotrophin, cooperatively regulate the adipogenic and lipolytic capacity of adipocytes. Metabolism *114*, 154430. https://doi.org/10.1016/j.metabol.2020.154430.

74. Xu, R., Vujić, N., Bianco, V., Reinisch, I., Kratky, D., Krstic, J., and Prokesch, A. (2024). Lipid-associated macrophages between aggravation and alleviation of metabolic diseases. Trends Endocrinol. Metab. *35*, 981–995. https://doi.org/10.1016/j.tem.2024.04.009.

75. Nicolás-Ávila, J.A., Pena-Couso, L., Muñoz-Cánoves, P., and Hidalgo, A. (2022). Macrophages, Metabolism and Heterophagy in the Heart. Circ. Res. *130*, 418–431. https://doi.org/10.1161/CIRCRESAHA.121.319812.

76. Guzik, T.J., Skiba, D.S., Touyz, R.M., and Harrison, D.G. (2017). The role of infiltrating immune cells in dysfunctional adipose tissue. Cardiovasc. Res. *113*, 1009–1023. https://doi.org/10.1093/cvr/cvx108.

77. Mangum, L.C., Hou, X., Borazjani, A., Lee, J.H., Ross, M.K., and Crow, J.A. (2018). Silencing carboxylesterase 1 in human THP-1 macrophages perturbs genes regulated by PPARgamma/RXR and RAR/RXR: down-regulation of CYP27A1-LXRalpha signaling. Biochem. J. *475*, 621–642. https://doi.org/10.1042/BCJ20180008.

78. Daemen, S., Gainullina, A., Kalugotla, G., He, L., Chan, M.M., Beals, J.W., Liss, K.H., Klein, S., Feldstein, A.E., Finck, B.N., et al. (2021). Dynamic Shifts in the Composition of Resident and Recruited Macrophages Influence Tissue Remodeling in NASH. Cell Rep. *34*, 108626. https://doi.org/10.1016/j.celrep.2020.108626.

79. Meng, Z., Qiu, X., Chen, Z., Lee, Y.t., Zhou, L., Lu, Y., Liu, T., Li, S., Levi, B., Gallagher, K.A., and Lin, J.D. (2025). Myeloid TGF-beta signaling shapes liver macrophage heterogeneity and metabolic liver disease pathogenesis. JHEP Rep. *7*, 101488. https://doi.org/10.1016/j.jhepr.2025.101488.

80. Li, X., Yang, L., Mao, Z., Pan, X., Zhao, Y., Gu, X., Eckel-Mahan, K., Zuo, Z., Tong, Q., Hartig, S.M., et al. (2020). Novel role of dynamin-related-protein 1 in dynamics of ER-lipid droplets in adipose tissue. FASEB J. *34*, 8265–8282. https://doi.org/10.1096/fj.201903100RR.

81. Lieu, E.L., Herman, M.A., and Hartig, S.M. (2025). Toward Scientific Rigor: Setting Standards for Indirect Calorimetry Analysis and Reporting. Diabetes *75*, 401–402. https://doi.org/10.2337/db25-0998.

82. Banks, A.S., Allison, D.B., Alquier, T., Ansarullah, Austad, S.N., Auwerx, J., Ayala, J.E., Baur, J.A., Carobbio, S., Churchill, G.A., et al. (2025). A consensus guide to preclinical indirect calorimetry experiments. Nat. Metab. *7*, 1765–1780. https://doi.org/10.1038/s42255-025-01360-4.

83. Li, G., Li, X., Mahmud, I., Ysaguirre, J., Fekry, B., Wang, S., Wei, B., Eckel-Mahan, K.L., Lorenzi, P.L., Lehner, R., and Sun, K. (2023). Interfering with lipid metabolism through targeting CES1 sensitizes hepatocellular carcinoma for chemotherapy. JCI Insight *8*, e163624. https://doi.org/10.1172/jci.insight.163624.

84. Li, G., Li, X., Yang, L., Wang, S., Dai, Y., Fekry, B., Veillon, L., Tan, L., Berdeaux, R., Eckel-Mahan, K., et al. (2022). Adipose tissue-specific ablation of Ces1d causes metabolic dysregulation in mice. Life Sci. Alliance *5*, e202101209. https://doi.org/10.26508/lsa.202101209.

85. Shao, L.J., Elizondo, F., Gao, F., Habib, R., Li, X., Pham, K., Ysaguirre, J., Elizondo, M., Shirazi, S., Eckel-Mahan, K.L., et al. (2025). Functional regulation of macrophages by Ces1d-Mediated lipid signaling in immunometabolism. Mol. Metab. *97*, 102166. https://doi.org/10.1016/j.molmet.2025.102166.

86. Li, X., Pham, K., Ysaguirre, J., Mahmud, I., Tan, L., Wei, B., Shao, L.J., Elizondo, M., Habib, R., Elizondo, F., et al. (2024). Mechanistic insights into metabolic function of dynamin-related protein 1. J. Lipid Res. *65*, 100633. https://doi.org/10.1016/j.jlr.2024.100633.

87. Goodman, L.D., Ralhan, I., Li, X., Lu, S., Moulton, M.J., Park, Y.J., Zhao, P., Kanca, O., Ghaderpour Taleghani, Z.S., Jacquemyn, J., et al. (2024). Tau is required for glial lipid droplet formation and resistance to neuronal oxidative stress. Nat. Neurosci. *27*, 1918–1933. https://doi.org/10.1038/s41593-024-01740-1.

88. Suganami, T., Nishida, J., and Ogawa, Y. (2005). A paracrine loop between adipocytes and macrophages aggravates inflammatory changes: role of free fatty acids and tumor necrosis factor alpha. Arterioscler. Thromb. Vasc. Biol. *25*, 2062–2068. https://doi.org/10.1161/01.ATV.0000183883.72263.13.

89. Bu, D., Crewe, C., Kusminski, C.M., Gordillo, R., Ghaben, A.L., Kim, M., Park, J., Deng, H., Xiong, W., Liu, X.Z., et al. (2019). Human endotrophin as a driver of malignant tumor growth. JCI Insight *5*, e125094. https://doi.org/10.1172/jci.insight.125094.

90. Doyle, S.E., O'Connell, R.M., Miranda, G.A., Vaidya, S.A., Chow, E.K., Liu, P.T., Suzuki, S., Suzuki, N., Modlin, R.L., Yeh, W.C., et al. (2004). Toll-like receptors induce a phagocytic gene program through p38. J. Exp. Med. *199*, 81–90. https://doi.org/10.1084/jem.20031237.

STAR★METHODS

KEY RESOURCES TABLE

REAGENT or RESOURCE	SOURCE	IDENTIFIER
Antibodies		
Anti-Perilipin-1 antibody	Abcam	Cat#ab61682; RRID:AB_944751
Anti-CD11c antibody [EP1347Y] - C-terminal	Abcam	Cat#ab52632; RRID:AB_2129793
MMP14 Polyclonal Antibody	Invitrogen	Cat#PA5-143023; RRID:AB_2933662
Galectin 3 Monoclonal Antibody (eBioM3/38 (M3/38)), Biotin, eBioscience™	Invitrogen	Cat#13-5301-82; RRID:AB_837113
Ces1d	Invitrogen	Cat#5–47802; RRID:AB_2606394
CD206 (MMR) Monoclonal Antibody (MR6F3)	Invitrogen	Cat#12 2061 82; RRID:AB_2637422
F4/80 Monoclonal Antibody (BM8), eFluor™ 450, eBioscience™	Invitrogen	Cat#48 4801 80; RRID:AB_1548756
NF-κB p65 (D14E12) Rabbit Monoclonal Antibody	Cell Signaling Technology	Cat#8242; RRID:AB_10859369
Phospho-NF-kappaB p65 (Ser536) (93H1) Rabbit Monoclonal Antibody	Cell Signaling Technology	Cat#3033; RRID: AB_331284
IL-1 beta (D3U3E) Rabbit Monoclonal Antibody	Cell Signaling Technology	Cat#12703; RRID: AB_2732782
IL-6 (D3K2N) Rabbit Monoclonal Antibody	Cell Signaling Technology	Cat#12153; RRID: AB_2898924
Acetyl-CoA Carboxylase 1 Antibody	Cell Signaling Technology	Cat#4190; RRID: AB_10547752
Phospho-Acetyl-CoA Carboxylase (Ser79) Antibody	Cell Signaling Technology	Cat#3661; RRID:AB_330337
HSL Antibody	Cell Signaling Technology	Cat#4107; RRID:AB_2296900
Phospho-HSL (Ser660) Antibody	Cell Signaling Technology	Cat#4126; RRID:AB_490997
Phospho-(Ser/Thr) PKA Substrate Antibody	Cell Signaling Technology	Cat#9621; RRID:AB_330304
beta-Actin (8H10D10) Mouse Monoclonal Antibody	Cell Signaling Technology	Cat#8H10D10; RRID:AB_2242334
ATGL Antibody (F-7)	Santa Cruz Biotechnology	Cat#sc-365278; RRID:AB_10859044
normal mouse IgG	Santa Cruz Biotechnology	Cat#sc-2025
Arginase-1 Antibody	Cell Signaling Technology	Cat#93668; RRID:AB_2800207
TNF alpha Antibody (TN3-19.12)	Santa Cruz Biotechnology	Cat#sc-12744; RRID: AB_628372
APC anti-mouse F4/80 Antibody	BioLegend	Cat#123115; RRID:AB_893493
APC anti-mouse CD11c Antibody	BioLegend	Cat#117310; RRID:AB_313779
FITC anti-mouse CD206 (MMR) Antibody	BioLegend	Cat#141704;RRID:AB_10901166
Alexa Fluor® 488 anti-mouse CD86 Antibody	BioLegend	Cat#105018; RRID:AB_493462
APC anti-mouse CD3 Antibody	BioLegend	Cat#100236; RRID:AB_2561456
PE anti-mouse CD4 Antibody	BioLegend	Cat#100408; RRID:AB_312693
Brilliant Violet 421™ anti-mouse CD8a Antibody	BioLegend	Cat#100738; RRID:AB_11204079
APOB Polyclonal Antibody	Proteintech	Cat#20578-1-AP; RRID:AB_10732938
Mouse MMR/CD206 Antibody	R&D Systems	Cat#MAB2535; RRID:AB_2063008
TREM2 Antibody (237920) [FITC]	Novus Biologicals	Cat#FAB17291F; RRID:AB_3116997
Alexa Fluor® 647 AffiniPure® Fab Fragment Donkey Anti-Goat IgG (H + L)	Jackson ImmunoResearch	Cat#705-607-003; RRID:AB_2340439

(*Continued on next page*)

Continued

REAGENT or RESOURCE	SOURCE	IDENTIFIER
HRP-conjugated goat anti-rabbit IgG	Santa Cruz Biotechnology	Cat#sc-2004; RRID:AB_631746
Alexa Fluor® 488 AffiniPure® F(ab')$_2$ Fragment Donkey Anti-Rabbit IgG (H + L)	Jackson ImmunoResearch	Cat#711-546-152; RRID:AB_2340619
IRDye 680RD Goat anti-Mouse IgG	LiCoR	Cat#926-68070
IRDye® 800CW Anti-Rabbit IgG	LiCoR	Cat#926-32213
IRDye® 800CW Anti-goat IgG	LiCoR	Cat#926-32214
IRDye® 800CW Anti-Rat IgG	LiCoR	Cat#926-32219
Rabbit Endotrophin antibody	Scherer Laboratory at UTSW	N/A
3A2 (MMP14 neutralizing antibody)	Gift from Xin Ge's laboratory at UTHealth	N/A
Chemicals, peptides, and recombinant proteins		
DMEM + GlutaMAX	Gibco	Cat#10569
DMEM	Gibco	Cat#21063
Fetal bovine serum	Thermo Fisher Scientific	Cat#A5670701
Accutase	Corning	Cat#25-058-C1
Antibiotics-Antimycotic (100x), Liquid	GenDEPOT	Cat#CA002-010
PowerUp SYBR Green Master Mix	Applied Biosystems	Cat#A25743
Brewer Thioglycollate Medium	Millipore Sigma	Cat#B2551-500 G
VECTASHIELD Vibrance® Antifade Mounting Medium with DAPI	Vector Laboratories	Cat#H-1800
Lipopolysaccharides from Escherichia coli O111:B4	Sigma-Aldrich	Cat#L4391-1MG
Oleic Acid	Sigma-Aldrich	Cat#4954-1GM
Palmitic Acid	Sigma-Aldrich	Cat#P0500
Lipoprotein, Low Density, Oxidized (LDL-ox)	Athens Bioscience, Inc	Cat#12-16-120412-OX
EDTA (0.5 M), pH 8.0, RNase-free	Invitrogen	Cat#AM9261
eBioscience™ 1X RBC Lysis Buffer	Invitrogen	Cat#00-4333-57
RIPA Lysis buffer, 10X	Millipore Sigma	Cat#20-188
Laemmli SDS sample buffer, reducing (6X)	Thermo Scientific	Cat# J61337.AD
Poly-L-Lysine Hydrobromide	Sigma-Aldrich	Cat#P4707
Paraformaldehyde 16% Aqueous Solution EM Grade	Electron Microscopy Sciences	Cat#15710-S
BODIPY™	Invitrogen	Cat#D3822
Albumin, Bovine, Cohn Fraction V, 98%, Cell Culture Grade, Low Endotoxin	Thermo Scientific	Cat#AAJ6509722
Bachem Endotrophin (mouse) Trifluoroacetate	Bachem	Cat#50-194-6734
TRIzol Reagent	Invitrogen	Cat#15-596-018
Insulin solution human	Sigma-Aldrich	Cat#I9278-5ML
Transferrin	Millipore Sigma	Cat#10652202001
Selenium	Millipore Sigma	Cat#229865
SuperSignal™ West Dura Extended Duration SUbstrate	Thermo Fisher Scientific	Cat#34076
Dexamethasone	Millipore Sigma	Cat#D4902
Critical commercial assays		
Free Fatty Acid (FFA) Assay Kit	BioAssay Systems	Cat#EFFA-100
Triglyceride (TAG) Assay Kit	Invitrogen	Cat#EEA028
Mouse IL-1 beta ELISA Kit	Sigma-Aldrich	Cat#RAB0274
Mouse IL-6 ELISA Kit	Sigma-Aldrich	Cat#RAB0308

(*Continued on next page*)

Continued

REAGENT or RESOURCE	SOURCE	IDENTIFIER
Mouse TNFα High Sensitivity ELISA Kit	Invitrogen	Cat#BMS607-2HS
Endotrophin ELISA Kit	Creative Diagnostics	Cat#DEIA-XYZ75
Phagocytosis Assay Kit (Green Zymosan)	Abcam	Cat#ab234053
cDNA kit High-Capacity cDNA Reverse Transcription Kit	Thermo Fisher Scientific	Cat#4368814
PureLink RNA Mini Kit	Ambion	Cat#12183025
Pierce Rapid Gold BCA Protein Assay Kit	ThermoFisher Scientific	Cat# A53225, A53226, A53227
Deposited data		
Raw and analyzed data	This paper	GSE335244
Experimental models: Cell Lines		
Alpha Mouse Liver: AML12 cells	ATCC	Cat#CRL-2254; RRID:CVCL_0140
Mouse: L929 cells	ATCC	Cat#CCL-1; RRID:CVCL_0462
Mouse: RAW264.7 cells	ATCC	Cat#Tib-71; RRID:CVCL_0493
Experimental models: Organisms/strains		
Mouse: C57BL/6J	The Jackson Laboratory	Strain #000664; RRID:IMSR_JAX:000664
Mouse: Lysm-Cre	The Jackson Laboratory	Strain #004781; RRID:IMSR_JAX:00478
Mouse: MMP14 $^{floxed/floxed}$ C57BL/6 mouse	Dr. Weiss Laboratory at the University of Michigan	N/A
Oligonucleotides		
Primers: MMP14 (Forward: TGGATACCCAATGCCCATTG, Reverse: CTTCGTCAAACACCCAGTGCTT)	Li et al.[42]	https://doi.org/10.1128/MCB.00564-19
Primers: Tlr4 (Forward: ATGGCATGGCTTACACCACC, Reverse: GAGGCCAATTTTGTCTCCACA)	Li et al.[42]	https://doi.org/10.1128/MCB.00564-19
Primers: Tgfbr1 (Forward: CGTGTGCCAAATGAAGAGGAT, Reverse: AAGGTGGTGCCCTCTGAAATG)	Li et al.[42]	https://doi.org/10.1128/MCB.00564-19
Primers: IL-6 (Forward: ACAACGATGATGCACTT, Reverse: CTTGGTCCTTAGCCACT)	Li et al.[42]	https://doi.org/10.1128/MCB.00564-19
Primers: IL-1b (Forward: CAACCAACAAGTGATATTCTCCATG, Reverse: GATCCACACTCTCCAGCTGCA)	Li et al.[42]	https://doi.org/10.1128/MCB.00564-19
Primers: Tnfa (Forward: GTGGAACTGGCAGAAGAGGC, Reverse: AGACAGAAGAGCGTGGTGGC)	Li et al.[42]	https://doi.org/10.1128/MCB.00564-19
Primers: Acc1 (Forward: CGCTCACCAACAGTAAGGTGG, Reverse: GCTTGGCAGGGAGTTCCTC)	Li et al.[80]	https://doi.org/10.1128/MCB.00564-19
Primers: Fasn (Forward: GGAGGTGGTGATAGCCGGTAT, Reverse: TGGGTAATCCATAGAGCCCAG)	Li et al.[80]	https://doi.org/10.1016/j.jlr.2024.100633
Primer: Scd1 (Forward: AGATCTCCAGTTCTTACACGACCAC, Reverse: GACGGATGTCTTCTTCCAGGTG)	Li et al.[80]	https://doi.org/10.1016/j.jlr.2024.100633
Primers: Srebp1 (Forward: ACTTCTGGAGACATCGCAAAA, Reverse: GGTAGACAACAGCCGCATC)	Li et al.[80]	https://doi.org/10.1016/j.jlr.2024.100633
Primers: Srebp2 (Forward: GCGTTCTGGAGACCATGGA, Reverse: ACAAAGTTGCTCTGAAAACAAATCA)	Li et al.[80]	https://doi.org/10.1016/j.jlr.2024.100633

(*Continued on next page*)

Continued

REAGENT or RESOURCE	SOURCE	IDENTIFIER
Primers: Trem2 (Forward: GCACCTCCAGGAATCAAGAG, Reverse: GGGTCCAGTGAGGATCTGAA)	Zhou et al.[63]	https://doi.org/10.1016/j.celrep.2025.115310
Primers: β-actin (Forward: GGCACCACACCTTCTACAATG, Reverse: GGGGTGTTGAAGGTCTCAAAC)	Li et al.[42,80]	https://doi.org/10.1128/MCB.00564-19
Software and algorithms		
Flowjo 10	FLOWJO,LLC	RRID:SCR_008520
Fiji-ImageJ	NIH	RRID:SCR_002285
PRISM 10.0	GraphPad Prism	RRID:SCR_002798
Adobe Photoshop	Adobe Inc.	RRID:SCR_014199
NIS Elements 5.21.00	Nikon	RRID:SCR_014329
CFX Maestro Software for Real-Time PCR Systems	Bio-Rad Laboratories	RRID:SCR_018064
BioRender	BioRender	RRID:SCR_018361
CalR	CalRapp	RRID:SCR_015849
Other		
Rodent Diet with 60kcal% Fat	Research Diets, Inc.	D12492i

EXPERIMENTAL MODEL AND STUDY PARTICIPANT DETAILS

Animals

All animal experiments were approved by the Animal Welfare Committee of the University of Texas Health Science Center at Houston (protocol number: AWC-24-0010) and conducted in accordance with NIH guidelines. Mice were housed in a specific pathogen–free facility under a 12-h light/12-h dark cycle at 22 ± 1°C with *ad libitum* access to food and water.

C57BL/6J mice (Jackson Laboratory, JAX #000664) were used as wild-type controls. *Mmp14*$^{flox/flox}$ mice (originally generated by Dr. Stephen Weiss's laboratory at University of Michigan) were maintained on a C57BL/6J background and crossed with LysM-Cre mice to generate myeloid-specific Mmp14 knockout mice (LysM-Cre; *Mmp14*$^{flox/flox}$; referred to as *Mmp14* KO). Littermate *Mmp14*$^{flox/flox}$ mice lacking Cre were used as wild-type (WT) controls.

Male mice were used for all studies. All mice were 8 weeks of age at the start of dietary interventions. For diet-induced obesity, age-matched WT and KO mice were fed a high-fat diet (HFD; 60% kcal from fat; Research Diet, #D12492i) for 16 weeks.[42] Body weight was recorded weekly. Body composition (fat mass and lean mass) was measured using an EchoMRI-100T system (Echo Medical Systems) and calculated per guidance.[81,82]

METHOD DETAILS

Body composition and indirect calorimetry

Body composition was assessed using an EchoMRI-100 system (Echo Medical Systems, Houston, TX, USA). Energy expenditure and metabolic parameters were measured by indirect calorimetry using PhenoMaster metabolic chambers (TSE Systems). Data were collected continuously over a 3-day period. Energy expenditure was calculated using Cal-R software in accordance with recently published guidelines for the analysis and interpretation of indirect calorimetry data.[81,82]

Glucose tolerance and insulin tolerance tests

The methods were revised from our previous publications.[35] For glucose tolerance tests (GTT), HFD-fed mice were fasted for 6 h and injected intraperitoneally with D-glucose (2.5 g/kg body weight). For insulin tolerance tests (ITT), mice were fasted for 4 h and injected intraperitoneally with insulin (0.75 U/kg for lean mice and 1.0 U/kg for HFD-fed mice). Blood glucose levels were measured from tail vein blood at indicated time points using a handheld glucometer.

Serum biochemistry

The methods were revised from our previous publications.[83,84] For serum lipid measurements, tail blood was collected into heparin-coated capillary tubes and centrifuged at 4,000 × g for 6 min. Free fatty acids (FFA; BioAssay Systems, EFFA-100), triglycerides (TAG; Invitrogen, EEA028), and total cholesterol (Cell Biolabs, STA-384)), IL-1β (Mouse IL-1 beta ELISA Kit, Sigma-Aldrich, RAB0274), IL-6 (Mouse IL-6 ELISA Kit, Sigma-Aldrich, RAB0308), TNFα (Mouse TNFα High Sensitivity ELISA Kit, Invitrogen,

BMS607-2HS) and endotrophin (endotrophin ELISA Kit, Creative Diagnostics, DEIA-XYZ75) were quantified using enzymatic assays according to the manufacturers' instructions. Lipid concentrations were normalized to protein concentration where applicable.

Tissue processing and histology

The histological methods were published previously.[83–85] Briefly, epididymal white adipose tissue (eWAT), subcutaneous white adipose tissue (sWAT), and liver were harvested immediately after euthanasia and fixed in 10% neutral-buffered formalin for 48 h at room temperature. Tissues were paraffin embedded, sectioned at 5 μm thickness, and stained with hematoxylin and eosin (H&E) or Masson's trichrome using standard protocols. Images were acquired using a brightfield microscope and analyzed in a blinded manner.

Immunofluorescence staining of tissue sections

The methods were published previously.[80,85–87] Briefly, paraffin sections were deparaffinized, rehydrated, and permeabilized in PBS containing 0.2% Triton X-100 for 10 min. Antigen retrieval was performed in sodium citrate buffer (pH 6.0) at 95°C for 30 min. Sections were blocked in PBS containing 5% bovine serum albumin (BSA) and incubated overnight at 4°C with primary antibodies against Mac2 (Galectin-3; eBioscience, 13-5301-82, clone M3/38, 1:100). After washing, sections were incubated with Alexa Fluor–conjugated secondary antibodies (Jackson ImmunoResearch, 1:500). APC-F4/80 (BM8) antibody (BioLegend, Cat# 123115) and FITC- TREM2 Antibody (Novus Biologicals, Cat# FAB17291F) were diluted in 3% BSA in 1 X PBST (1:100) to identify the lipid-associated macrophages. Nuclei were counterstained with DAPI, sections were mounted with antifade mounting medium (Vector Laboratories, H-1800), and images were acquired using a Nikon AXR confocal microscope.

eWAT-conditioned medium preparation

The conditions were adapted from a previously published method.[88] Specifically, eWAT was harvested from male mice fed either a standard chow diet (~10% kcal from fat) or a high-fat diet (~60% kcal from fat) for 6 weeks. Tissue was minced into ~2–3 mm fragments and incubated in serum-free DMEM supplemented with 1% fatty acid–free BSA at 37°C for 24 h. Conditioned medium (CM) was collected, filtered through a 70 μm strainer, centrifuged to remove debris, and diluted 1:4 with complete culture medium before use (designated CM-L or CM-H).

Cell culture and treatments

All the cell culture conditions have been established by previous publications.[57,80,85] Raw264.7 macrophages were cultured in DMEM supplemented with 10% fetal bovine serum (FBS) and 1% penicillin/streptomycin. AML12 hepatocytes were cultured in DMEM/F12 supplemented with 10% FBS, insulin (5 μg/mL), transferrin (5 μg/mL), selenium (5 ng/mL), and dexamethasone (40 ng/mL). L929 fibroblasts were cultured in DMEM + GlutaMAX (Gibco) to generate macrophage colony stimulating factor (M-CSF)–containing conditioned medium. The MMP14-neutralizing monoclonal antibody 3A2 (1μg/ml) or isotype-matched control IgG was used at indicated dilutions for *in vitro* experiments, as we previously reported.[42] The concentration for endotrophin to treat the macrophages was 1μg/ml.[89] LPS (100 ng/mL) and IL-4 (50 ng/mL) were added to the culture medium, and macrophages were treated for 24 h before being harvested for analysis.

Isolation of Brewer Thioglycollate-elicited peritoneal macrophages

To obtain elicited peritoneal macrophages, both Chow-fed and 16-week-HFD-fed mice were given an intraperitoneal injection of 3% Brewer Thioglycollate medium (Millipore Cat #B2551-500G) solution to promote macrophage accumulation in the peritoneal cavity. Peritoneal cells were collected 4 days after injection by lavage with cold sterile PBS. The recovered cells were centrifuged, resuspended in complete culture medium, and seeded onto culture plates. After allowing macrophages to adhere for 12 h, non-adherent cells were removed by washing, and the adherent macrophage population was used for subsequent experiments. The isolated cells were defined as Brewer Thioglycollate-elicited peritoneal macrophages.

eWAT-resident macrophage isolation

The resident macrophages in the HFD-fed WT and *Mmp14* KO mice were isolated from the SVF of eWAT. Briefly, adipose tissue was minced, digested with collagenase at 37°C, filtered through a cell strainer, and centrifuged to collect the SVF pellet. After red blood cell lysis and washing, macrophages were enriched from SVF cells using anti-F4/80 magnetic beads. The isolated macrophages were washed with cold PBS and lysed in protein extraction buffer containing protease and phosphatase inhibitors for subsequent Western blot analysis.

Bone marrow–derived macrophage (BMDM) differentiation and treatment

The approach has been recently published.[85] Briefly, bone marrow was flushed from femurs and tibias of WT and KO mice using sterile DMEM, filtered through 70 μm strainers, and centrifuged at 400 × g for 5 min. Cells were cultured in DMEM + GlutaMAX supplemented with 10% FBS, 20% L929-conditioned medium, and antibiotics. After 7 days, adherent macrophages were harvested using Accutase and replated for experiments. MMP14 deletion was confirmed by immunoblotting. LPS (100 ng/mL) and IL-4 (50 ng/mL) were added to the culture medium, and differentiated macrophages were treated for 24 h before being harvested for analysis.

Lipid droplet staining

Cells were incubated with BODIPY 493/503 (2 μM; Invitrogen, D3922) for 20 min at 37°C, washed with PBS, fixed in 4% paraformaldehyde, and imaged using a Nikon AXR confocal microscope.[80]

Migration assays

Scratch-wound assays were performed on confluent monolayers of Raw264.7 cells or BMDMs based on our previous method.[85] Cells were serum-starved for 6 h, scratched using a sterile pipette tip, washed, and treated with LPS (100 ng/mL), oleic acid (3.5 μM), palmitic acid (5 μM), or CM(L)/CM(H) for 40 h. Images were acquired at 0 and 40 h, and migration was quantified using ImageJ.

Phagocytosis assays

Phagocytosis was assessed using green fluorescent zymosan particles, according to a previous publication[90] (Abcam, ab234053). In brief, BMDMs were incubated with particles for 3 h, washed, quenched, and fluorescence was measured at Ex/Em = 490/520 nm using a plate reader. Data were normalized to controls.

Flow cytometry

Stromal vascular fraction (SVF) cells were isolated from eWAT by collagenase digestion. Cells were blocked with Fc receptor blocker and stained with antibodies against F4/80 (Thermo Fisher, 48-4801-80), CD11c (BioLegend, 117310), CD206 (BioLegend, 141704), CD3 (BioLegend, 100236), CD4 (BioLegend, 100408), and CD8a (BioLegend, 100738). To identify lipid-associated macrophages (LAMs), cells were stained with APC-conjugated anti-F4/80 antibody (clone BM8; BioLegend, Cat# 123115) and FITC-conjugated anti-TREM2 antibody (Novus Biologicals, Cat# FAB17291F), each used at 0.25 μL per 50 μL of FACS buffer. Unless otherwise specified, antibodies were diluted 1:50 in cold FACS buffer (1% BSA in PBS) for flow cytometric analysis. Data were acquired on a BD FACSymphony A1 or Cytek Aurora and analyzed using FlowJo software (V10).[85]

Western blotting

Tissues and cells were lysed in RIPA buffer supplemented with protease and phosphatase inhibitors. Proteins were separated by SDS–PAGE, transferred to PVDF membranes, and probed with antibodies against MMP14 (Invitrogen; Abcam ab51074, 1:1000), ATGL (Santa Cruz sc-36527, 1:1000), ACC/p-ACC (Cell Signaling 4190/3661, 1:2500), HSL/p-HSL (Cell Signaling 4107/4126, 1:2500), PLIN1 (Abcam ab61682, 1:5000), Ces1d (Invitrogen 5–47802, 1:2500), endotrophin (Dr. Philipp Scherer's lab, 1:2000), NF-κB p65 (Cell Signaling 8242, 1:2500), p–NFκB S536 (Cell Signaling 3033, 1:2500), TNFα (Cell Signaling 372, 1:2500), IL-1β (Cell Signaling 12703, 1:2500), IL-6 (Cell Signaling 12153, 1:2500), and β-actin (BD Biosciences 61256, 1:1000). Signals were detected using IRDye secondary antibodies (LI-COR, 1:10,000) and quantified using Image Studio or ImageJ (Version 1.51 23). Specifically for Arg1 (Cell Signaling 93668, 1:1000), signals were detected by chemiluminescent detection (ECL) using horseradish peroxidase (HRP) conjugated second antibody (goat anti-rabbit, Santa Cruz Biotechnology, sc-2004). The images were achieved by a Bio-Rad ChemiDoc Touch Imaging System (Version 2.3.0.07).

RNA sequencing

Raw264.7 cells were treated with LPS (100 ng/mL) ± MMP14-neutralizing antibody (3A2) for 24 h. Total RNA was isolated using TRIzol and subjected to rRNA depletion, strand-specific library preparation, and paired-end 150-bp sequencing on an Illumina NovaSeq X platform. Library quality was assessed using an Agilent Bioanalyzer, and sequencing was performed at the Cancer Genomics Center, UTHealth Houston. Differential expression analysis was performed using standard. FASTQ files were aligned to the Genome Reference Consortium Human Build 38 (GRCh38) using HISAT2, and transcript assembly was performed using the Pluto RNA-seq pipeline. Raw count data were converted to normalized counts expressed as counts per million (CPM). Differential expression analysis was performed using R packages including edgeR, pheatmap, ggplot2, and RColorBrewer. *p* values were calculated using unpaired, two-tailed Student's *t* test. Pathway enrichment analysis was conducted using Gene Set Enrichment Analysis (GSEA). *p* values were calculated using unpaired, two-tailed Student's *t* test.

Quantitative PCR

Total RNA was reverse transcribed using RevertAid Reverse Transcriptase (Thermo Fisher). qPCR was performed using SYBR Green chemistry on a Bio-Rad CFX96 system. Expression levels were normalized to β-actin and calculated using the ΔΔCt method.[57]

Statistical analysis

Unless otherwise indicated, data are presented as mean ± SEM. Statistical analyses were performed as described in the figure legends. n represents biologically independent animals or independent cell culture experiments. For comparisons between two groups, two-tailed Student's *t* test was used. For comparisons among multiple groups, one-way or two-way ANOVA followed by appropriate post hoc multiple-comparison testing was used. Statistical significance is indicated as follows: n.s., not significant; $^{*}p < 0.05$; $^{**}p < 0.01$; $^{***}p < 0.001$; $^{****}p < 0.0001$.